A CFD-sectional algorithm for population balance equation coupled with multi-dimensional flow dynamics

Xiaopeng Shang, Man Pun Wan, Bing Feng Ng*, Shirun Ding
School of Mechanical and Aerospace Engineering, Nanyang Technological University, Singapore
*corresponding author: bingfeng@ntu.edu.sg
Telephone: +65 67904163

ABSTRACT

The sectional methodology has become a powerful tool for population balance modeling. However, in coupling with the computational fluid dynamics (CFD), there exist several challenges, including the complex double integrals associated with the sectional coefficients, the serious computational burden in the solution of a large number of partial differential equations, and the nonlinear and coupled source terms. In the present study, a novel CFD-sectional algorithm that aims at addressing these challenges is developed in the open-source package – OpenFOAM to solve population balance equation coupled with multi-dimensional flow dynamics. The sectional coefficients are specified by a numerical quadrature with adaptive adjustment of integration limits. The inter-equation coupling is treated by hybrid-segregated procedures and the source term is formally linearized by the operator splitting method. The numerical quadrature proves to be computationally efficient and accurate in solving the sectional coefficients. The developed CFD-sectional algorithm is validated against a self-preserving solution of particles undergoing Brownian coagulation. The acoustic agglomeration in a standing wave is simulated as a representative case study. It has been demonstrated that the predictions regarding the particle size distribution and agglomeration process agree well with the experimental data, which verifies the capability of the present CFD-sectional algorithm in simulating the spatially inhomogeneous population balance equation coupled with multi-dimensional flows.

Keywords: population balance modeling; sectional method; computational fluid dynamics (CFD); coalescence/agglomeration; acoustic agglomeration

1. Introduction

Population balance modeling is of great importance in a wide spectrum of particulate processes, ranging from combustion, spraying, nano-powder synthesis, to granulation etc. [1-7]. Although the population balance equation (PBE) is dependent on both time and space in nature, numerical simulations of PBE traditionally assume that the aerosol is homogeneous within the geometric boundaries, indicating that all the properties of the aerosol are identical everywhere without spatial variation of any quantity involved in the process [8]. Under such circumstances, the PBE can only capture the temporal evolution of the particle size distribution (PSD), which is the so-called temporal model. The temporal PBE is a partial integro-differential equation and has only a limited number of known analytical solutions. As such, approximate solutions to the temporal PBE are often determined by using several numerical approaches, which can be classified as the method of moments [3, 4, 9-11], Monte Carlo method [12-14], the sectional method [15-17] and the fixed pivot method or cell average method [18-20]. The temporal model can explore some basic characteristics of the particulate system, however, its application is restricted by the homogeneity assumption to a limited number of scenarios since most of aerosol systems in industrial engineering or laboratory experiments are spatially inhomogeneous, i.e., multi-dimensional. In addition, the temporal PBE does not take into account any coupling of the aerosol processes with the fluid flow or heat transfer, which limits its ability to achieve the complete information of particulate laden flows. Therefore, the tempo-spatial formulation of the PBE must be solved by coupling with a computational fluid dynamics (CFD) framework to reveal the essential features of aerosol dynamics in a realistic multi-dimensional flow.

In the CFD-based population balance modeling, all the physical variables involved need to be discretized in three spatial directions in addition to the temporal and internal coordinates. This greatly increases the complexity of the algorithm and thus, compared to the extensive numerical simulations of the temporal model, only a limited number of studies have been reported to solve the spatially multi-dimensional population balance equation in the presence of fluid flows. Stratmann and Whitby [21] pioneered a preliminary numerical solution for the combined CFD-population balance modeling of aerosol dynamics by extending computational heat transfer and fluid flow codes. Kruis et al. [22] simplified the population balance equation based on a mean particle size, and developed a monodisperse population balance (MPB) model. Buddhiraju and Runkana [23] simulated the nanoparticle synthesis in a flame reactor by the CFD-MPB model, and their prediction was basically in agreement with the experimental data. In spite of the robustness, simplicity and computation efficiency, the MPB model fails to give sufficient insights to the particle characteristics and deteriorates the simulation quality for polydisperse aerosols [24]. In general, the population balance equations by using the method of moments (MOM) are not closed when modeling the size-dependent aerosol process with coagulation or breakage [9]. Several approaches are introduced to solve the closure problem, of which the most common includes assuming a specific functional form of the particle size distribution *a priori*, and quadrature approximation such as quadrature method of moments (QMOM). Schwade and Roth [25] solved the tempo-spatial PBE for aerosol dynamics via the moment methodology based on the assumption of a unimodal lognormal size distribution. However, in most engineering applications, the particle size distribution of an aerosol may not be known beforehand and its functional form may be changed with time or space. Thus, the QMOM is more versatile and promising in the context of moment based methods. Passalacqua et al. [26] constructed a PBE solver based on the extended quadrature method of moments (EQMOM) and then coupled it to a standard CFD code package in OpenFOAM, which enables the solution of the PBE for inhomogeneous systems with transport of particles due to the fluid motion. Although the moment methodology presents the advantage of being less demanding on computational resources, it is plagued by the assumption of a specific particle size distribution or the inversion problem that arises in the reconstruction of the distribution details from the moment integrals. In addition, it is reported that the realizability cannot be guaranteed for a scheme higher than second-order based on the reconstruction of moments [27]. Another method to resolve the PBE is through the use of the stochastic method or Monte Carlo (MC) method. Liu and Chan [13] developed a coupled CFD-Monte Carlo method to simulate the complex aerosol dynamics in turbulent flows at different Reynolds numbers. The major limitation of this method is the extremely high computation cost since the time step is required to be small, and the tracking of individual particles is computationally complicated.

Fan et al. [28] adopted the MC method to simulate a typical case of acoustic agglomeration in a small physical space with only 7,650 particles but the computation time was up to 4 days on a computer equipped with 4 CPUs (Intel i5) and RAM of 8192 MB.

The sectional method, first proposed by Gelbard and Seinfeld [15], has been extensively used in the simulation of particulate systems. This method divides the continuous particle size distribution into a finite number of discrete sections, and within each section the particle distribution can be regarded as uniform or of any pre-defined function. The sectional method is advantageous due to the visual representation of the particle distribution and direct comparison with the experimental measurements. Plus, implementation of the sectional method in an Eulerian computational fluid dynamics framework is conceptually straightforward. Pyykonene and Jokineimi [29] constructed two CFD-based sectional schemes of population balance modeling coupled with fluid flows, one based on boundary layer type streamtube methodology and the other on full Eulerian representation. However, their full Eulerian sectional scheme failed to provide accurate predictions due to excessive demands on grid resolution. Jeong and Choi [30, 31] analyzed the growth of non-spherical polydisperse particles in a two-dimensional geometry by solving two sets of sectional PBEs coupled with detailed fluid dynamics calculations. Spatial transport phenomena such as convection, diffusion, thermophoresis and deposition were accounted for and comparisons have been made between the calculations using spatially two-dimensional approach and simplified one-dimensional approach, and the experimental data. It has been demonstrated that at high flow rates, the simplified one-dimensional approach would result in significant errors in comparison with the two-dimensional approach. Frederix et al. [32] applied the characteristics-based sectional method to the complete set of fluid equations for a compressible flow by incorporating the fractional step method. However, the feasibility of the developed algorithm was only demonstrated in studying the aerosol nucleation and condensation and did not cover the coagulation/agglomeration process. In addition, the variant of the sectional method, discrete-sectional method, has also been widely used in combination with CFD for the chemical synthesis of monomers and subsequent Brownian coagulation [33, 34].

Although the sectional methodology has become a powerful technique for population balance modeling, there exist several challenges or limitations in the current CFD-sectional algorithm: a) The sectional coefficients have to be solved via numerical quadrature of complex integrals while accurate evaluation of these integrals is computationally demanding, especially for the particles with a wide range of size spectrum. b) To obtain the refined particle size distribution, one has to solve a vast number of partial differential equations (PDEs). c) The source terms in the sectional PBE associated with the coagulation or agglomeration process are strongly nonlinear and coupled. As such, when conceiving the CFD-sectional algorithm, any inappropriate treatment can undermine the convergence and stability of the solution, especially for the ultrafast coagulation/agglomeration such as acoustic agglomeration. In view of the above challenges and limitations, the CFD-sectional method for spatially inhomogeneous population balance modeling in inhomogeneous flows remains to be an attractive topic.

In the present study, we develop a novel CFD-sectional algorithm for univariate population balance modeling in a multi-dimensional laminar or turbulent flow, targeting at settling the challenges in the existing sectional simulations. The sectional formulation of the PBE, which incorporates the convective and diffusive transport of aerosols, is constructed based on the sectional method of Gelbard and Seinfeld [15] and the coagulation/agglomeration kernel is present as an additional source term. A modified numerical integration scheme is proposed to improve the computation efficiency and accuracy in the calculation of the sectional coefficients. Subsequently, the framework of population balance modeling is described with focus on the processing of the inter-equation coupling and nonlinearity of the source terms. The sectional modeling of PBE is incorporated to a standard CFD algorithm in the open-source code library – OpenFOAM. The analytical solution of a self-preserving Brownian coagulation is chosen to validate the developed computer codes. A case study is carried out to simulate the acoustic agglomeration in a standing wave field and the numerical results are compared with experimental data to demonstrate the capability of the present CFD-sectional algorithm.

2. Sectional formulation of the population balance equation

The tempo-spatial evolution of particle size distribution for aerosols with coagulation or agglomeration process is governed by the population balance equation [35],

$$\frac{\partial n(\vec{x},v,t)}{\partial t} + \nabla \cdot \left[\vec{U} n(\vec{x},v,t)\right] = \nabla \cdot \left[D \nabla n(\vec{x},v,t)\right] + S \qquad (1)$$

where, the particle size distribution function $n(\vec{x},v,t)$ is dependent on the space vector $\vec{x}$, time t and particle volume v. U is the velocity of particles due to convective transport and D is the diffusion coefficient or diffusivity.

The source term S describes the net increase of aerosol particles due to the coagulation/agglomeration process [35],

$$S = \frac{1}{2}\int_0^v \beta(\hat{v}, v-\hat{v}) n(\vec{x},\hat{v}) n(\vec{x}, v-\hat{v}) d\hat{v} - \int_0^\infty \beta(v,\hat{v}) n(\vec{x},v) n(\vec{x},\hat{v}) d\hat{v} \qquad (2)$$

where β is the kernel or frequency function in the coagulation/agglomeration process.

Following the notation of Gelbard and Seinfeld [15], a general property of an aerosol is introduced as

$$q(\vec{x},v,t) = \alpha v^\gamma n(\vec{x},v,t) \qquad (3)$$

where, α and γ are constants that determine the general property of an aerosol (number, volume or surface area concentration etc.).

Dividing the entire particle size domain into a finite number of sections, one can define a discrete quantity of the aerosol in the l-th section as

$$Q_l = \int_{v_{l-1}}^{v_l} q(\vec{x},v,t) dv = \int_{v_{l-1}}^{v_l} \alpha v^\gamma n(\vec{x},v,t) dv \qquad (4)$$

where, for α=1 and γ=0, Q_l is the particle number concentration N_l, while for α=1, γ=1, Q_l is the particle volume concentration, V_l.

By applying Eq. (4) to the population balance equation Eq. (1), the sectional formulation for a general quantity of the aerosol in the l-th section can be written as follows

$$\frac{\partial Q_l}{\partial t} + \nabla \cdot \left(\vec{U} Q_l\right) = \nabla \cdot \left(\bar{D}_l \nabla Q_l\right) + S_l \qquad (5)$$

The sectional formulation of the source term in the l-th section, S_l, which results from the coagulation/agglomeration process, is written as

$$S_l = \frac{1}{2}\sum_{i=1}^{l-1}\sum_{j=1}^{l-1} {}^1\beta_{i,j,l} Q_i Q_j - \sum_{i=1}^{l-1} {}^2\beta_{i,l} Q_i Q_l - \frac{1}{2}\, {}^3\beta_{l,l} Q_l^2 - \sum_{i=l+1}^{NS} {}^4\beta_{i,l} Q_i Q_l \qquad (6)$$

where *NS* is the number of sections, and the sectional coefficients, ${}^1\beta_{i,j,l}$, ${}^2\beta_{i,l}$, ${}^3\beta_{l,l}$ and ${}^4\beta_{i,l}$, represent the inter- and intra-sectional coagulation/agglomeration rates between sections prior to the *l*-th section, between the *l*-th section and lower sections, within the *l*-th section and between the *l*-th section and higher sections, respectively.

Often, the aerosol size distribution is not restrictively described by the particle volume *u* or *v* but the size variable ξ or ζ, which is a function of the particle volume, $\xi = f(u)$ or $\zeta = f(v)$. In this situation, the particle size distribution is sectionalized on the basis of the size variable ξ or ζ and accordingly the sectional coefficients are solved on ξ or ζ. The detailed formulas of the sectional coefficients are demonstrated in Table 1, which can also be referred to [15].

Table 1. Formulas of the sectional coefficients, $\zeta_i = f(v_i)$, $u = f^{-1}(\xi)$ and $v = f^{-1}(\zeta)$.

${}^1\beta_{i,j,l}$	$\int_{\zeta_{i-1}}^{\zeta_i}\int_{\zeta_{j-1}}^{\zeta_j} \frac{\theta(v_{l-1} < u+v < v_l)(u+v)^\gamma \beta(u,v,\vec{x})}{\alpha u^\gamma v^\gamma (\zeta_i-\zeta_{i-1})(\zeta_j-\zeta_{j-1})} d\xi d\zeta$
${}^2\beta_{i,l}$	$\int_{\zeta_{i-1}}^{\zeta_i}\int_{\zeta_{l-1}}^{\zeta_l} \frac{[\theta(u+v > v_l)u^\gamma - \theta(u+v < v_l)((u+v)^\gamma - u^\gamma)]\beta(u,v,\vec{x})}{\alpha u^\gamma v^\gamma (\zeta_i-\zeta_{i-1})(\zeta_l-\zeta_{l-1})} d\xi d\zeta$
${}^3\beta_{l,l}$	$\int_{\zeta_{l-1}}^{\zeta_l}\int_{\zeta_{l-1}}^{\zeta_l} \frac{[\theta(u+v > v_l)(u^\gamma + v^\gamma) + \theta(u+v < v_l)((u^\gamma + v^\gamma) - (u+v)^\gamma)]\beta(u,v,\vec{x})}{\alpha u^\gamma v^\gamma (\zeta_l-\zeta_{l-1})(\zeta_l-\zeta_{l-1})} d\xi d\zeta$
${}^4\beta_{i,l}$	$\int_{\zeta_{i-1}}^{\zeta_i}\int_{\zeta_{l-1}}^{\zeta_l} \frac{u^\gamma \beta(u,v,\vec{x})}{\alpha u^\gamma v^\gamma (\zeta_i-\zeta_{i-1})(\zeta_l-\zeta_{l-1})} d\xi d\zeta$

Many of the general moments of a particle size distribution appear in the expressions for the integral properties of a particulate system. Four moments correspond to four common properties of an aerosol. The zeroth, second, third and sixth moment are proportional to the total number, total surface area, total volume and total volume square per unit space, respectively. Therefore, the corresponding set of sectional equations conserving the zeroth, second, third and sixth moment is called the *n*-model, *s*-model, *v*-model and *v*^{2}-model, respectively. The sectional method based on Gelbard and Seinfeld [15] can conserve one moment or property provided that the corresponding model is solved and it is straightforward to conserve multiple moments via solving several models simultaneously. Adams and Seinfeld

[36] proposed the two-moment aerosol sectional (TOMAS) model which can conserves the total number as well as total volume. Kajino et al. [37] extended it to a triple-moment sectional (TMS) model by incorporating the total surface area. However, by this way, the number of the sectional equations to be solved will be doubled or tripled, which is very demanding on computation capacity. Thus, the present CFD-sectional solver does not incorporate the multiple-moment model, and the other moments or properties can be derived based on the conserved moment or property [38]. Wu and Biswas [39] reported that for the derived moments, the deviation caused by internal inconsistency is not significant if small values of sectioning space can be adopted, and they recommended the *v*-model with better performance of deriving other properties. Vanni [40] made similar conclusion via the *v*-model in terms of the comparative analysis of the number averaged particle size and the volume/mass averaged particle size. Therefore, the present CFD-sectional solver selects the *v*-model which satisfies the volume/mass conservation.

3. Numerical solution of the sectional population balance equation

Different from the general scalar transport equation, the sectional PBE requires special attention to challenges involved in the evaluation of sectional coefficients, discretization of both the external and internal coordinates as well as the solution process. In this part, we will firstly introduce a modified numerical integration scheme with adaptive integration limits which can evaluate the sectional coefficients accurately and efficiently. Then the framework of discretizing and solving the sectional PBE will be described with focus on the treatment of the inter-equation coupling and nonlinearities lying in the source terms.

3.1. Specification of sectional coefficients

The sectional coefficients in Table 1 represent the probabilities that a pair of sections, such as the *i*-th and *j*-th section, collide with each other and form agglomerates lying within or out of a given "goal" particle size region, which is specified by the discontinuous function ϑ. Gelbard and Seinfeld [15] proposed a numerical scheme for geometric sectionalization under which the upper limit of a section is at least twice its lower limit, i.e., $v_{i+1} \geq 2v_i$. However, their scheme involves very complex formulas to eliminate the discontinuity from the integrands, and even the dummy variables are introduced into the integration limits. This substantially complicates the solution of the sectional coefficients via the numerical integration. Herein, a numerical integration scheme modified by the adaptive adjustment of integration limits is presented for geometric sectionalization which has high accuracy and efficiency.

For the integrals in Table 1, the integration domain with original upper and lower limits is a rectangular region determined by the section boundary in the *u*-*v* coordinate system. However, the "goal" region which is meaningful in the integration is irregular due to the discontinuous functions. As shown in Fig. 1, the "goal" region of the numerical integration for ${}^{1}\beta_{i,j,l}$ is actually the trapezoidal black area which is bounded by the straight lines $u + v = v_{l-1}$ and $u + v = v_l$. In the case that the difference between the sizes of two colliding particles is very large, the two sections which the two particles belong to will go far away from each other. In fact, for a particle which is ten times larger than the other one in diameter, the volume is a thousand times apart. Consequently, the integration domain is seriously skewed so that the "meaningful" "goal" region is insignificant compared to the whole integration domain. As such, for the numerical integration with original integration limits, most of the interpolating nodes make no contributions with very coarse nodes in the "goal" region. Therefore, a standard numerical quadrature may cause serious computation errors and cannot be applied directly.

The geometric constraint implies that at least one of the colliding particles which forms an agglomerate in the *l*-th section must be in the *(l-1)*-th section, which means that ${}^{1}\beta_{i,j,l} = 0$ for the section pairs of $i < l - 1, j < l - 1$. Since ${}^{1}\beta_{i,j,l}$ represents the "birth" rate between sections prior to the *l*-th section, i.e., $i \leq l - 1, j \leq l - 1$, the condition $u + v < v_l$ is automatically satisfied. The other condition $u + v > v_{l-1}$ determines the lower limit of *v* coordinate for the case of $i = l - 1, j < l - 1$, or the lower limit of *u* coordinate for the case of $i < l - 1, j = l - 1$. As shown in Fig. 1a for the case of $i = l - 1, j < l - 1$, in the presence of the discontinuous function, the lower limit of *v* coordinate cannot be smaller than the intersection point denoted by the purple circle marker while the *u* coordinate will not change. Hence, the integration limits can be adjusted adaptively according to the intersection point determined by the discontinuous function. To include the case of $i = l - 1, j = l - 1$, the integration limits of ${}^{1}\beta_{i,j,l}$ can be adjusted to $\left[\max\left(v_{l-1}-v_j, v_{i-1}\right), v_i\right]$ for *v* coordinate and left unchanged for *u* coordinate. Under such situation, most of the "meaningless" region is eliminated from the original integration domain and the integration domain is modified as the sum of the black "goal" region and the grey triangle region. For the same number of interpolating nodes, this modified numerical integration scheme can increase the resolutions in the "goal" region, which avoids a waste of the computation resources and greatly improves the accuracy of the numerical integration. For the case of $i < l-1, j = l-1$, the limits of integration become $\left[\max\left(v_{l-1}-v_i, v_{j-1}\right), v_j\right]$ for *u* coordinate and remain unchanged for *v* coordinate. Similarly, the integration limits for ${}^{2}\beta_{i,l}$ and ${}^{3}\beta_{l,l}$ can also be adaptively adjusted according to the intersection points as shown in Fig. 2 and Fig. 3. In the calculation of ${}^{2}\beta_{i,l}$ the two terms of the integrands represented by two discontinuous functions are split into two integrals; when calculating ${}^{3}\beta_{l,l}$, the term with the discontinuous function, $u+v>v_l$, is obtained by its complementary integral described by $u+v<v_l$. The results are tabulated in Table 2 for programming basis.

Table 2. The integration limits with adaptive adjustment for the modified numerical integration scheme.

		Discontinuous Function	New Integration Limits	
			u coordinate	*v* coordinate
${}^{1}\beta_{i,j,l}$	$i = l-1$	$\theta(v_{l-1} < u+v < v_l)$	(v_{j-1}, v_j)	$\left[\max\left(v_{l-1}-v_j, v_{i-1}\right), v_i\right]$
	$j = l-1$	$\theta(v_{l-1} < u+v < v_l)$	$\left[\max\left(v_{l-1}-v_i, v_{j-1}\right), v_j\right]$	(v_{i-1}, v_i)
${}^{2}\beta_{i,l}$		$\theta(u+v > v_l)$	$(v_l - v_i, v_l)$	(v_{i-1}, v_i)
		$\theta(u+v < v_l)$	$(v_{l-1}, v_l - v_{i-1})$	(v_{i-1}, v_i)
${}^{3}\beta_{l,l}$		$\theta(u+v < v_l)$	$(v_{l-1}, v_l - v_{l-1})$	$(v_{l-1}, v_l - v_{l-1})$
		$\theta(u+v > v_l)$	$1-\theta(u+v < v_l)$	
${}^{4}\beta_{i,l}$		N.A.	N.A.	N.A.

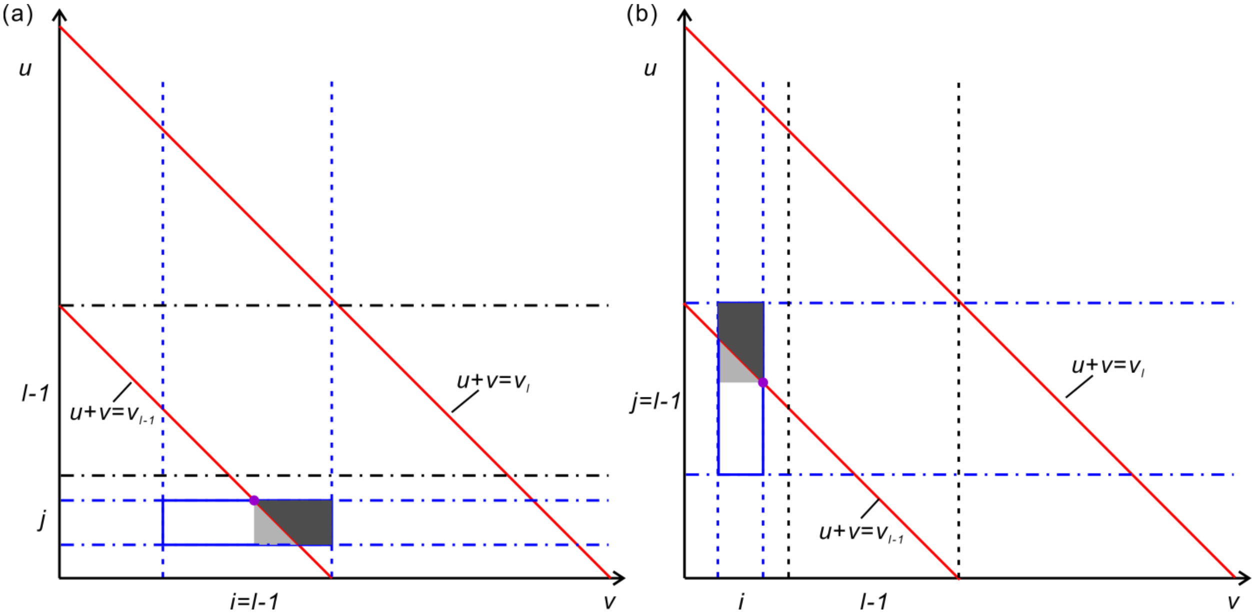

Fig. 1. Illustration of the integration limits of ${}^{1}\beta_{i,j,l}$ for the case of: (a) $i = l - 1, j < l - 1$ and (b) $i < l - 1, j = l - 1$. The black shaded area shows the "goal" region and v_{l-1} and v_l represent the lower and upper boundaries of the agglomerating section.

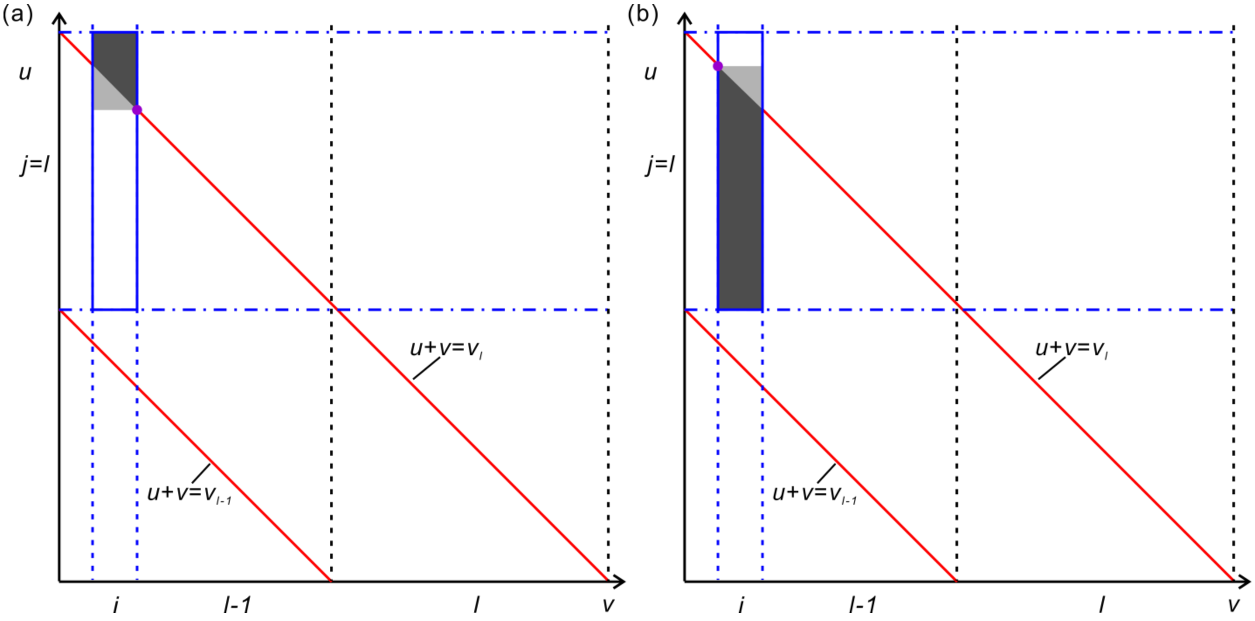

Fig. 2. Illustration of the integration limits of ${}^{2}\beta_{i,l}$ for the case of: (a) $\theta(u + v > v_l)$ and (b) $\theta(v_{l-1} < u + v < v_l)$. The black shaded area shows the "goal" region and v_{l-1} and v_l represent the lower and upper boundaries of the agglomerating section.

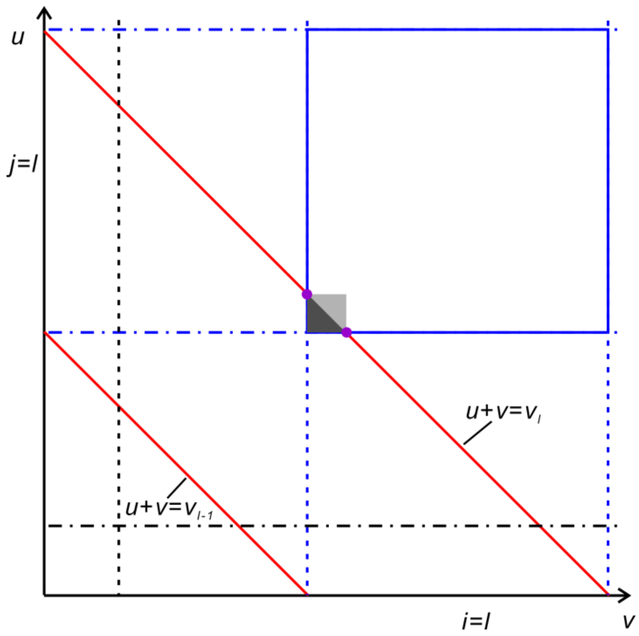

Fig. 3. Illustration of the integration limits of ${}^{3}\beta_{l,l}$. The black shaded area shows the “goal” region and v_{l-1} and v_l represent the lower and upper boundaries of the agglomerating section.

The sectional coefficients can be solved by some kind of numerical quadrature such as composite Newton-Cotes quadrature modified by the adaptive integration limits in Table 2. The numerical integration formulation of a sectional coefficient for Newton-Cotes quadrature can be represented by

$$I = \iint_R F(u,v)dudv = \sum\sum \lambda_{ij}F_{ij} \tag{7}$$

where $F(u,v)$ is the discontinuous integrand, R is the integration domain after being adaptively adjusted, λ_{ij} is a matrix of coefficients corresponding to the quadrature formula such as Trapezoid rule or Simpson’s rule and F_{ij} is the value at the interpolating node which is calculated by

$$F_{ij} = \begin{cases} \beta(u_j, v_i), & \theta\ function\ is\ satisfied \\ 0, & others \end{cases} \tag{8}$$

The proposed numerical integration scheme with the adaptive adjustment of integration limits can achieve high accuracy and economic consumption of computation resource. In the meantime the complexity of this scheme is greatly alleviated compared to that of Gelbard and Seinfeld [15] and the programming for the numerical integration is very straightforward.

3.2. Convection term

We must specify the local velocity components of a non-uniform flow field before proceeding to discretize the convection term of the sectional population balance equation. Thus, the solution procedure of the sectional PBE should be embedded into a CFD program such as the SIMPLE algorithm proposed by Patankar [41] for steady-state problems or PISO algorithm proposed by Issa [42] for transient problems. The SIMPLE or PISO scheme consists of a repeated loop of momentum predictor, pressure solution, and velocity correction and the details can be referred to [41, 42]. With the conservative fluxes or velocity fields, the convection term in sectional PBE is linear and thus the discretization does not present particular problems when the traditional Gauss upwind is used. We will describe how to incorporate the solution procedure of sectional PBE into SIMPLE or PISO loop in Section 4.

3.3. Diffusion term

In a laminar particle laden flow, the diffusion of particles results from the random Brownian motion and this is called Brownian diffusion. However, in addition to the Brownian motion, the particles in a turbulent flow also move with the irregular turbulent fluctuations, which is the so-called turbulent diffusion. It has been shown that Fick's law can be applied to turbulent diffusion just as it does to Brownian diffusion [43]. Hence, in a turbulent flow the diffusion term can be modeled simply by the regular formulation $\nabla \cdot (D\nabla n)$ except that the diffusivity D is the sum of Brownian diffusivity D_B and turbulent diffusivity D_T, i.e., $D = D_B + D_T$.

The Brownian diffusivity, D_B, is calculated by the well-known Stokes-Einstein equation with Cunningham coefficient [44],

$$D_B\left(d_p\right) = \frac{k_B T C_C}{3\pi\mu d_p} \tag{9}$$

where the Cunningham coefficient C_C is calculated by

$$C_C = 1 + Kn[A + B\exp(-C/Kn)] \tag{10}$$

where, A, B and C are three constants, A=1.257, B=0.4 and C=1.1, and the Knudsen number $Kn=2\lambda/d_p$, and λ is the free path of air molecules. In the continuum regime, the Cunningham coefficient is equal to unity.

Depending on the flow conditions such as the Reynolds number (*Re*), the turbulent diffusion of particles can be several orders of magnitude more intense than Brownian diffusion. In turbulent flows, particles are usually caused by their inertia to lag behind or to shoot ahead of the local fluid motion (at random). However, on the average, these tendencies cancel out, which means that the root mean square (RMS) fluctuating velocity of particles is equal to the turbulent velocity of the local fluid. Thus the turbulent diffusivity of the particles can be assumed to equal the local turbulent or eddy viscosity, which means that $D_T = \nu_t$, where, ν_t is the turbulent or eddy viscosity [43].

For the Reynolds Averaged Simulation (RAS) turbulence modeling, the turbulent viscosity can be calculated according to the turbulent characteristics,

$$\nu_t = C_\mu \frac{k^2}{\varepsilon} \tag{11}$$

where, C_μ is a constant, $C_\mu = 0.09$, k the turbulent kinetic energy and ε energy dissipation rate.

Since the diffusivity D is dependent on the particle size, the sectional formulation of the diffusion term in the population balance equation is, in fact, described by,

$$\int_{v_{l-1}}^{v_l} \alpha v^\gamma \nabla \cdot [D(v)\nabla n] dv = \nabla \cdot \int_{v_{l-1}}^{v_l} \alpha v^\gamma [D(v)\nabla n] dv \tag{12}$$

To decouple the integrand in Eq. (12), the sectional diffusivity is regarded as a constant in each section, e.g., its average value,

$$\overline{D}_l = \frac{1}{v_l - v_{l-1}} \int_{v_{l-1}}^{v_l} D(v) dv \tag{13}$$

Then, the diffusion term can be sectionalized as

$$\int_{v_{l-1}}^{v_l} \alpha v^\gamma \nabla \cdot [D(v)\nabla n] dv = \nabla \cdot \left[\overline{D}_l \int_{v_{l-1}}^{v_l} \alpha v^\gamma \nabla n dv\right] = \nabla \cdot (\overline{D}_l \nabla Q_l) \tag{14}$$

which is exactly the first term on the right hand side in the sectional population balance equation. As a typical Laplacian term, the sectional diffusion term Eq. (14) is usually discretized by the Gauss central differencing scheme.

3.4. Source term

Let us return to Eqs. (5) and (6) for the sectional population balance equation. It can be seen that the source term of the PDE for the *l*-th section is a function of all the dependent variables, $Q_1 \cdots Q_{NS}$, and highly coupled with the PDEs in the other sections. Thus, the solution of each unknown involves all the other dependent variables. However, the particle size range of interest is usually divided into tens of sections and each section generates one unknown. Thus, a simultaneous solution of all unknowns is not preferred due to the tremendous cost of computation resource. When we solve the coupled PDEs in sequence, the inter-equation coupling associated with the source terms must be handled at first.

A simple method to decouple the source term is that we substitute “old” values of the initial guess or in the previous loop for all the other variables expect Q_l,

$$S_l = \frac{1}{2}\sum_{i=1}^{l-1}\sum_{j=1}^{l-1} {}^{1}\beta_{i,j,l} Q_i^o Q_j^o - \sum_{i=1}^{l-1} {}^{2}\beta_{i,l} Q_i^o Q_l - \frac{1}{2}\, {}^{3}\beta_{l,l} Q_l^2 - \sum_{i=l+1}^{NS} {}^{4}\beta_{i,l} Q_i^o Q_l \tag{15}$$

where, a superscript “o” denotes the “old” values. In this manner, the solution of the PDEs is fully segregated in a SIMPLE or PISO loop, which means that the inter-equation couplings among the variables $Q_1 \cdots Q_{NS}$ would always be lagged in the solution process. This lagging effect will, of course, reduce the speed of convergence and also bring about an error source, which will be serious in transient flows due to the error accumulation with the time marching.

Herein, in the calculation of the *l*-th section, Q_l, the other variables involved are treated in a hybrid-segregated way: the variables, $Q_1 \cdots Q_{l-1}$, adopt the “new” values which have been updated in the current loop while the other unknown variables adopt the “old” values in the last loop. Such a hybrid-segregated computation scheme can be expressed by,

$$S_l = \frac{1}{2}\sum_{i=1}^{l-1}\sum_{j=1}^{l-1} {}^{1}\beta_{i,j,l} Q_i^n Q_j^n - \sum_{i=1}^{l-1} {}^{2}\beta_{i,l} Q_i^n Q_l - \frac{1}{2}\, {}^{3}\beta_{l,l} Q_l^2 - \sum_{i=l+1}^{NS} {}^{4}\beta_{i,l} Q_i^o Q_l \tag{16}$$

where the superscript “n” denotes the “new” value which has been updated in the current loop. By this method, the source term in the first equation of Q_1 is calculated by the “old” values of all the variables in the previous loop and then the value of Q_1 is updated; the source term in the second equation of Q_2 is calculated by the updated Q_1 and the “old” values of the other variables in the previous loop and then the value of Q_2 is updated. Following this line, the source term in the *l*-th equation of Q_l is obtained by the updated variables from the sections prior to the *l*-th section and the "old" values of the variables after the *l*-th section. In practice, after all the dependent variables $Q_1 \cdots Q_{NS}$ are obtained, one more solution procedure will be repeated as a correction process: the intermediate solution from the preceding step is employed instead of the solution from the last loop. Obviously, this two-stage hybrid-segregated scheme establishes a closer inter-equation coupling and is capable of avoiding the lagging effect considerably.

Another difficulty associated with the sectional population balance equation arises from the nonlinearity present in the source term. Inside each loop, the PDE is discretized in the computation domain and the resultant discretization equation is solved by iterative methods. However, the source term of the *l*-th section, S_l, is a nonlinear quadratic function of Q_l even though all the other variables are substituted by either "new" or "old" values in the previous or current loop. The nonlinear source term leads to troubles in constructing the discretization equation and also fails to employ the existing linear algebraic techniques. Thus the source term needs to be linearized before we proceed to construct and solve the discretization equation.

The simplest manner of linearizing the source term is to treat it as a constant irrespective of the iteration process, which is termed the explicit technique. This means that the source term is evaluated by the value of the dependent variable Q_l in the previous loop and keeps unchanged in the iteration process. This approach is acceptable only if the source is constant or relatively insignificant in comparison with other terms in the equation. However, for the ultra-fast coagulation/agglomeration processes such as acoustic agglomeration the source term is dominant in the equation, and the explicit technique has the issues of sluggish convergence and instability. In spite of unconditionally stability, on the other hand, the implicit technique is also not advisable having in mind the complexity of nonlinear solvers and computational efforts required. Thus, we can formally account for a linear dependence by decomposing the source term into the sum of an explicit part and an implicit part in the iterations which combines the merits of computational efficiency of explicit schemes and stability of implicit schemes. This technique is also termed as operator splitting method or fractional step method [14, 42, 45].

We denote the values of the previous iteration with a superscript "*" to distinguish them from the values of the previous loop. The source term at the current iteration can be linearized via a first-order Taylor series,

$$S_l = S_l(Q_l^*) + \left(\frac{\partial S_l}{\partial Q_l}\right)^* (Q_l - Q_l^*) = \underbrace{\left(\frac{\partial S_l}{\partial Q_l}\right)^* Q_l}_{Implict} + \underbrace{S_l(Q_l^*) - \left(\frac{\partial S_l}{\partial Q_l}\right)^* Q_l^*}_{Explicit} \tag{17}$$

where, the first term is an implicit part and the second and third term are explicit. This linearized form of the source term satisfies the method recommended by Patankar [41], which can be written as

$$S = S_C + \phi_P S_P \tag{18}$$

where, S is the source term S_l, ϕ_P is the dependent variable Q_l at the present computation node P, S_P is the coefficient of ϕ_P and S_C is a constant.

Substituting Eq. (16) into Eq. (17), we can immediately obtain,

$$S_l = \underbrace{\left(- {}^3\beta_{l,l} Q_l^* - \sum_{i=1}^{l-1} {}^2\beta_{i,l} Q_i^n - \sum_{i=l+1}^{NS} {}^4\beta_{i,l} Q_i^o\right)}_{S_P} Q_l + \underbrace{\frac{1}{2}\, {}^3\beta_{l,l} (Q_l^*)^2 + \frac{1}{2} \sum_{i=1}^{l-1} \sum_{j=1}^{l-1} {}^1\beta_{i,j,l} Q_i^n Q_j^n}_{S_C} \tag{19}$$

where, S_C and S_P are expressed by

$$S_C = \frac{1}{2}\, {}^3\beta_{l,l} (Q_l^*)^2 + \frac{1}{2} \sum_{i=1}^{l-1} \sum_{j=1}^{l-1} {}^1\beta_{i,j,l} Q_i^n Q_j^n \tag{20a}$$

$$S_P = - {}^3\beta_{l,l} Q_l^* - \sum_{i=1}^{l-1} {}^2\beta_{i,l} Q_i^n - \sum_{i=l+1}^{NS} {}^4\beta_{i,l} Q_i^o \tag{20b}$$

However, updating the value of Q_l in every iteration indicates frequent access to CPU and the memory. This will slow down the computation speed tremendously and cause enormous burden of computation considering the large number of PDEs to be solved at all the computation nodes. In practice, we use the value of Q_l in the previous loop as a constant to evaluate the coefficients of linearization S_C and S_P until the next loop. In this way, the source term is calculated by

$$S_l = \underbrace{\left(- {}^{3}\beta_{l,l} Q_l^o - \sum_{i=1}^{l-1} {}^{2}\beta_{i,l} Q_i^n - \sum_{i=l+1}^{NS} {}^{4}\beta_{i,l} Q_i^o\right)}_{S_P} Q_l + \underbrace{\frac{1}{2}\, {}^{3}\beta_{l,l} (Q_l^o)^2 + \frac{1}{2} \sum_{i=1}^{l-1} \sum_{j=1}^{l-1} {}^{1}\beta_{i,j,l} Q_i^n Q_j^n}_{S_C} \tag{21}$$

This linearization scheme is computationally efficient and stable with the splitting of implicit and explicit terms. It can also be seen that the implicit part of the source term is always negative-sloped ($S_P < 0$), which increases the diagonal dominance of the resultant matrix of discretization equations and guarantees convergence and boundedness of the solution [46].

3.5 Solution of the sectional population balance equation

The sectional population balance equations are discretized by a finite volume based scheme and then solved by a linear algebraic solver in OpenFOAM. For transient problems, the temporal discretization is fulfilled by the Euler implicit method which guarantees boundedness and unconditional stability. When setting the boundary conditions, the wall can be regarded as perfectly absorbing with the value of Q_l equal to zero or impenetrable with the flux of Q_l equal to zero. The iterative solution procedure to solve the algebraic equations is the stabilized preconditioned bi-conjugate gradient (PBiCGStab), originally proposed by Van der Vorst [47]. In fact, the program in OpenFOAM supports the run-time selection (RTS) mechanism which enables the user to choose the discretization and solution schemes at a point of program execution [48]. The sectional population equation is solved in sequence from the first section to the last one with the decoupling of the source terms. Finally, the information regarding a general property of the aerosol is obtained for the complete set of particle size sections of interest.

The numerical methods of solving population balance equation are generally classified as the moment method, the Monte Carlo method and the discrete method. The moment method is superior in the low demands on the computational resources and relatively simple mathematical form for implementation. However, the inversion problem arises in the reconstruction of the distribution details from moment integrals [*]. Plus, an additional limitation is usually imposed to the maximum time steps to address the realizability issue when the moment method is implemented in the Eulerian framework [*]. The Monte Carlo method is easy to incorporate multiple internal coordinates and can capture the history and trajectory of particles. However, the Monte Carlo method tracks the dynamics of each individual particle and thus compared to other methods, the computation is extremely expensive in computation time and memory usage [*]. The sectional method, as one typical discrete method, is able to give the direct representation of the particle size distribution, and its computation cost is moderate, falling in between the moment method and the Monte Carlo method. Moreover, the solution process of the sectional method is conceptually straightforward in the finite-volume simulations and the "realizability" issue can be simply circumvented [*]. However, since each size bin gives rise to one discrete population balance equation, the computation may be very expensive in time and memory when a large number of size bins are used.

4. Description of the CFD-sectional algorithm

The solution procedure for the sectional PBE can be embedded into a typical CFD scheme such as the SIMPLE algorithm for steady-state problems or PISO algorithm for transient problems, which allows us to study the aerosol dynamics in a complex flow field. Additionally, the functionality of the CFD-sectional solver can be leveraged by incorporating with the thermal or turbulence models in OpenFOAM.

We shall describe the solution procedures of the CFD-sectional algorithm for the PBE coupled with incompressible flow equations (i.e., continuity equation and momentum equation) and focus on the solution of the sectional PBE. The important procedures can be summarized as follows:

1) Set up the initial conditions and boundary conditions for all the field variables.

2) Go through the SIMPLE loop for steady state flows or the PISO loop for transient flows:

2a) Solution of pressure-velocity systems;

2b) Solution of other transport equations such as turbulent quantities if present;

2c) Solve the sectional coefficients via the modified numerical integration;

2d) Calculate the sectional diffusivity (Brownian diffusivity and turbulent diffusivity if present);

2e) Calculate the coefficients of linearization S_C and S_P using the “new” values for the lower sections and the “old” values for the current or higher sections;

2f) Linearize the source term by splitting it into the sum of implicit and explicit parts;

2g) Solve the sectional population balance equation via a linear algebraic iteration technique;

2h) Proceed to the next section until the sectional PBE is solved for all sections;

2i) Repeat the solution procedure from 2d) to 2h) to obtain the corrected solutions.

3) If the convergence criterion or the final time step is not reached, return to step 2).

It is to be noted that the step 2c) can be executed out of the SIMPLE or PISO loop if the sectional coefficients are independent on the flow characteristics or fluid properties. The flowchart of the developed CFD-sectional solver is illustrated in Fig. 4. The solution of flow equations for the velocity-pressure system is represented by *U* Equation and *p* Equation, and the solution process of the sectional population balance equation is represented by *Q* Equation. The standard *k*-*ε* model, which introduces two extra transport equations for turbulent kinetic energy, *k* Equation and turbulent dissipation rate, *ε* Equation, is selected for Reynolds-averaged simulation (RAS) turbulence modeling.

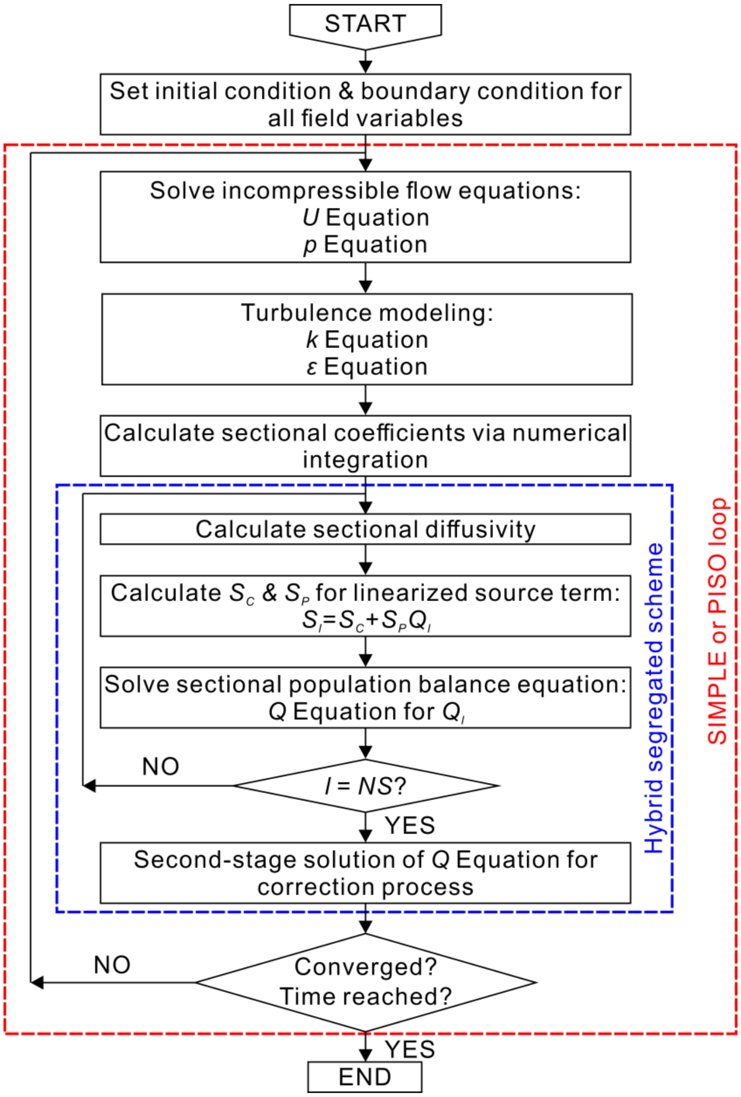

Fig. 4. Schematic representation of the CFD-sectional algorithm.

5. Results and Discussion

5.1. Validation of the CFD-sectional algorithm

5.1.1. The modified numerical integration

To improve the computation efficiency and accuracy, the sectional coefficients are solved by some numerical quadrature which is modified by adaptively adjusting the integration limits corresponding to the discontinuous functions. In this section, we will examine the improvement of the modified numerical integration by considering a simple situation where Q_l represents the particle number concentration N_l, and the kernel is equal to a constant. Under such situation, the sectional coefficients in Table 1 can be directly figured out with exact values. Without loss of generality, the kernel is regarded as equal to unity, and then the sectional coefficients are equal to the ratio of the area of the "goal" region determined by the discontinuous functions to the area of the original rectangle as shown in Fig. 1-3. The detailed expressions for the numerical integrals and exact values of the sectional coefficients when $Q_l = N_l$ and $\beta = 1$ are listed in the Supplementary Material.

Let us take an exemplary size domain of $\zeta = log_{10}[d_p(\mu m)] = (-1.05, 1.05)$ divided by 20 sections. The sectional coefficients are solved by the composite Simpson quadrature for the same number of integration nodes with and without the adaptive integration limits. ${}^1\beta_{i,j,20}$, the "birth" rate of the particles in the 20-th section, is investigated as an example. For such a geometric sectioning scheme, ${}^1\beta_{i,j,20}$ is equal to zero when $i < 19, j < 19$ because at least one of a pair of colliding particles is required to come from the 19-th section to generate a resultant particle in the 20-th section as aforementioned. Thus, the selected results for $i = 19, j = 1,3 \cdots 19$ can be presented in Table 3 as the representative values of ${}^1\beta_{i,j,20}$ since ${}^1\beta_{i,j,20} = {}^1\beta_{j,i,20}$. It can be seen that the results of the numerical integration without adaptive limits are basically coincident with the exact values for $j > 13$ but deviate seriously from the exact values for $j \leq 13$. Obviously, the deviation from exact values is increased when the *j*-th section goes far away from the 19-th section. Especially, when *j* is smaller than 11, there will be only one integration node lying inside the "goal" region, leading to a constant with a serious error of computation. With the adjusted integration limits, the modified numerical integration gives rise to satisfactory results and the relative error is much smaller than 1% for all pairs of colliding sections, which indicates that the accuracy of the calculation is greatly improved and the adaptive adjustment of the integration limits effectively relieves the computation error caused by the skewness of colliding sections.

Table 3. Selected ${}^1\beta_{19,j,20}$ calculated by numerical integration with and without adaptive limits.

j	ζ	*v* (μm^3)	Exact	Beta1-W/	Error-W/ (%)	Beta1-W/O	Error-W/O (%)
1	-0.945	7.656E-22	3.076E-06	3.076E-06	0.003	3.333E-03	108274.865
3	-0.735	3.266E-21	1.312E-05	1.312E-05	0.003	3.333E-03	25305.548
5	-0.525	1.393E-20	5.597E-05	5.597E-05	0.003	3.333E-03	5855.642

7	-0.315	5.943E-20	2.388E-04	2.388E-04	0.004	3.333E-03	1296.139
9	-0.105	2.535E-19	1.018E-03	1.019E-03	0.004	3.333E-03	227.287
11	0.105	1.081E-18	4.345E-03	4.345E-03	0.003	3.333E-03	23.276
13	0.315	4.613E-18	1.853E-02	1.853E-02	0.003	1.922E-02	3.718
15	0.525	1.968E-17	7.906E-02	7.906E-02	0.003	7.918E-02	0.151
17	0.735	8.395E-17	3.372E-01	3.373E-01	0.003	3.372E-01	0.008
19	0.945	3.581E-16	9.981E-01	9.979E-01	0.026	9.979E-01	0.026

5.1.2. Validation against analytical solution of Brownian coagulation/agglomeration

We validate the present CFD-sectional algorithm against an analytical solution of the self-preserving distribution of an aerosol undergoing Brownian coagulation/agglomeration. Lee et al. [49] studied the change of particle size distribution caused by Brownian coagulation/agglomeration in the continuum regime, and obtained a self-preserving analytical solution for the size distribution of an initially lognormal distribution.

The self-preserving particle size distribution in terms of the logarithmic coordinates of the particle diameter is described by

$$n_p(\zeta,t)=\frac{dN}{dv}\frac{dv}{d\zeta}=\frac{\ln(10)N(t)}{\sqrt{2\pi}\ln\sigma(t)}\exp\left\{-\frac{\ln^2[d_p/d_{pg}]}{2\ln^2\sigma(t)}\right\} \tag{22}$$

where, ζ is the size variable, $\zeta=log_{10}d_p=log_{10}\left[(6v/\pi)^{1/3}\right]$. At the time t, the total number concentration $N(t)$, the geometric mean particle diameter d_{pg}, and the geometric standard deviation $\sigma(t)$ are described by [49],

$$\frac{N(t)}{N_0}=\frac{1}{1+[1+\exp(\ln^2\sigma_0)]KN_0t} \tag{23a}$$

$$\left(\frac{d_{pg}}{d_{pg0}}\right)^3=\frac{\exp\left(\frac{9}{2}\ln^2\sigma_0\right)\{1+[1+\exp(\ln^2\sigma_0)KN_0t]\}}{\langle 2+\{\exp(9\ln^2\sigma_0)-2\}/\{1+[1+\exp(\ln^2\sigma_0)]KN_0t\}\rangle^{1/2}} \tag{23b}$$

$$\ln^2\sigma(t)=\frac{1}{9}\ln\left[2+\frac{\exp(9\ln^2\sigma_0)-2}{1+[1+\exp(\ln^2\sigma_0)]KN_0t}\right] \tag{23c}$$

where K is a constant, $K=2k_BT/3\mu$, and N_0, d_{pg0} and σ_0 are the initial values for $N(t)$, d_{pg} and $\sigma(t)$, respectively.

The evolution of an aerosol with particles undergoing Brownian coagulation/agglomeration in the continuum regime is simulated by the CFD-sectional solver with the kernel described by,

$$\beta(u,v) = \frac{2k_BT}{3\mu}\left[(u)^{1/3} + (v)^{1/3}\right]\left[\frac{1}{(u)^{1/3}} + \frac{1}{(v)^{1/3}}\right] \tag{24}$$

where the Cunningham coefficient is equal to unity in the continuum regime. For comparison with the analytical solution, the flow velocity is set to zero and the aerosol is homogeneous in space. The operation temperature for Brownian coagulation is 293 K. The aerosol at the initial time is log-normal with a geometric mean diameter of 1 μm and standard deviation of 2.5. The number concentration N_0 at the inlet is 10^{10} particles/m^3 and the particle density is 1,000 kg/m^3. The simulation was performed in parallel on a workstation equipped with 8 CPUs (Intel i7) and the tolerance is 1e-6 for all variables. The CPU time is 14,058 seconds for the computation domain of 10,000 grids to complete 48 hours of physical time. The simulation results were compared against those of the CFD-fixed pivot model in terms of the computation time, accuracy and algorithm complexity. To be in line with the analytical solution, the number density function for the CFD-fixed pivot method is calculated by $\bar{n}_i = N_i/(v_i - v_{i-1})$ for the *i*-th size bin, where N_i is the number concentration, and v_{i-1} and v_i are size bin boundaries.

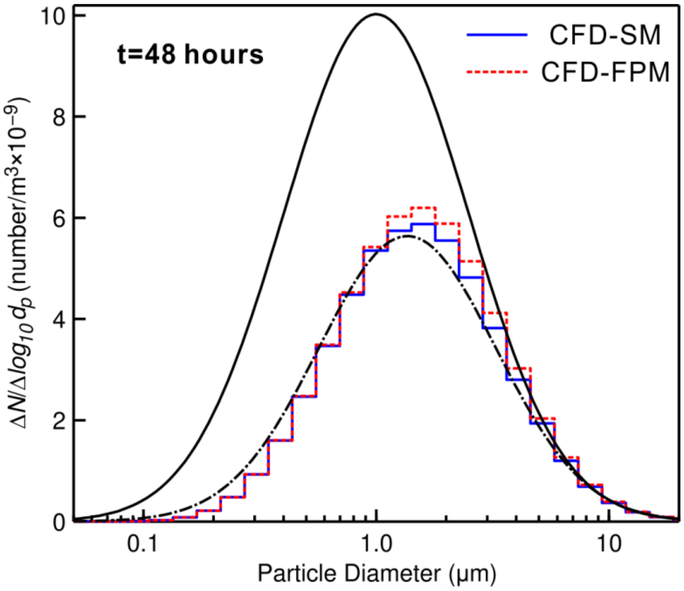

Fig. 5. Comparison between the self-preserving particle distribution (dash-dotted line) and the simulation results predicted by the CFD-sectional method (solid stairs) and the CFD-fixed pivot method (dashed stairs) for an aerosol of particles undergoing Brownian coagulation in the continuum regime at 48 hours. The initial distribution is denoted by the solid line.

The particle size distributions predicted by the present CFD-sectional method (solid stairs) and the CFD-fixed pivot method (dashed stairs) at 48 hours are compared with the analytical solution (dash-dotted line) and the initial distribution (solid line) in Fig. 5. It can be observed that the particle size distributions predicted by both methods match the analytical solution of the self-preserving distribution very well, and the discrepancy between simulations and exact solutions is expected to become smaller when wider particle size range is considered. The satisfactory agreement verifies the accuracy of the present CFD-sectional approach and computation codes in the solution of the population balance equation. It is also noticeable that the CFD-sectional simulation shows better agreement with the self-preserving solution than the CFD-fixed pivot method. As shown in Table 4, the geometric mean diameter and geometric standard deviation are 1.489 μm and 2.274 for the CFD-sectional simulation, and 1.527 μm and 2.267 for the CFD-fixed pivot method, compared to 1.362 μm and 2.406 for the analytical self-preserving solution, respectively. Obviously, the CFD-sectional method has higher accuracy than the CFD-fixed pivot method with the same number of size bins (sections or pivots).

Table 4. Comparison of the numerical results predicted by the CFD-sectional method and CFD-fixed pivot method.

Model	Geometric Mean Diameter		Geometric Standard Deviation		CPU Time (second)
	d_g (μm)	Error (%)	σ	Error (%)	
Analytical	1.362	N.A.	2.406	N.A.	N.A.
CFD-SM	1.489	9.32%	2.274	5.49%	14,058
CFD-FPM	1.527	12.11%	2.267	5.78%	9,430

Both the sectional method and the fixed pivot method are based on the discrete method while the major difference lies in the pre-defined functional form within each size bin. As shown in Fig. *a, the sectional method assumes that the particle size distribution is uniformly distributed within each size bin, indicating that the assumed distribution function in the *i*-th size bin is given by, $n_i(v,t) = N_i/\Delta v_i \cdot (v_{i-1} \leq v \leq v_i)$, where, N_i is the number concentration, $\Delta v_i = v_i - v_{i-1}$ is the width of the *i*-th size bin. The fixed pivot method, as shown in Fig. b, assumes that the particle distribution within each size bin is concentrated at a representative size or pivot in the spirit of point mass, which means that the distribution function is a singular point function, $n_i(v,t) = N_i\delta(v - v_{mi})$, where, v_{mi} is the pivot and δ is the Dirac delta function, with $\delta = \infty$

when $v = v_{mi}$ and otherwise $\delta = 0$. Theoretically, the uniform distribution assumed by the sectional method provides higher-order accuracy than the singular point distribution at pivots in the fixed pivot technique. Thus, the CFD-sectional simulation shows better agreement with the self-preserving solutions than the CFD-fixed pivot method. However, due to the complex functional form of the particle distribution, the solution of the sectional coefficients involves troublesome numerical quadrature of double integrals with discontinuous integrands for the sectional method. In contrast, the reassignment coefficients (equivalent to sectional coefficients) of the fixed pivot method can be easily solved via simple algebraic operations. Thus, in spite of the modified numerical quadrature with adaptive integration limits, the CFD-sectional method demands more computation time than the CFD-fixed pivot method as shown in Table 4.

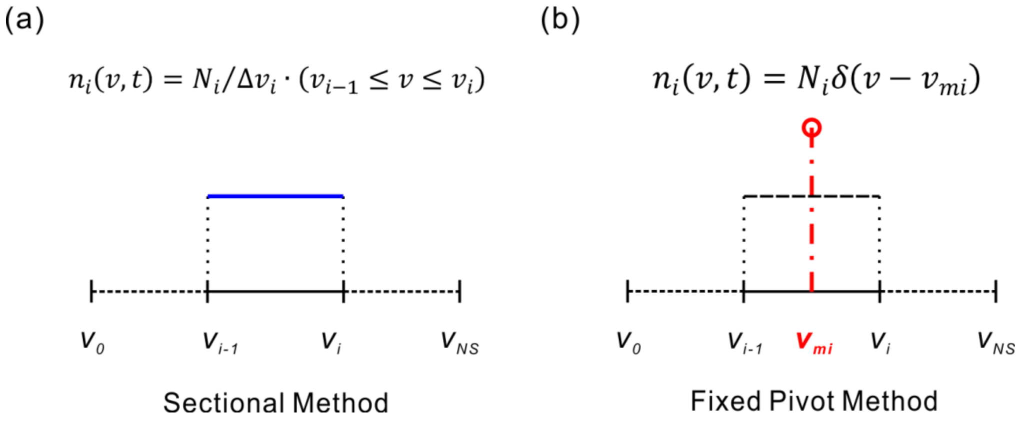

Sectional Method

Fixed Pivot Method

Fig. 6. Illustration of the sectional method (a) and the fixed pivot method (b).

The zeroth, second, third and sixth moments of a particle size distribution are proportional to the total number, total surface area, total volume and total volume square of particles per unit space, respectively. The present CFD-sectional solver conserves the total volume/mass, and the other properties can be derived readily based on the *v*-model [38, 39]. It can be seen in Table 5 that the approximate values of the derived properties based on the volume-conserved model are in accordance with the analytical solution for both low-order and high-order properties, and the errors are 0.200%, 1.923% and 1.997%, for the total number, *N*, total surface area, *S* and total volume square, v^2, respectively. Thus, the present solver is shown to have excellent performance in terms of the three common derived properties or moments. Generally, the accuracy of the sectional method is determined by a combination of many factors, such as the sectional coefficients, the discretization scheme, the internal consistency and sectioning space. The present study justifies that for the derived moments or properties, the deviation caused by the internal inconsistency is not significant if the sectioning space is fine enough [39]. Vanni [40] made similar conclusion via the comparison of the number averaged particle size and the volume/mass averaged particle size.

Table 5. Comparison of total number, total surface area and total volume square per unit space between the analytical solution and the derived values based on the CFD-sectional solver.

	N (particles/unit space)	*S* (m^2/unit space)	v^2 (m^6/unit space)
CFD-sectional	6.992E9	0.159	5.515E-21
Analytical Solution	7.006E9	0.156	5.407E-21
Error	0.200%	1.923%	1.997%

5.2. Case study of acoustic agglomeration

Acoustic agglomeration, in recent years, has gained world-wide attention, as an efficient preconditioning technique in air conditioning systems [17, 50-53]. Under the action of a sound field, small particles in a suspension collide with one another to form large agglomerates and as a result, the efficiency of conventional particle removal technologies is greatly improved. The particle size distribution can shift significantly to larger particulates within a short time of several seconds in the acoustic chamber, which indicates that the acoustic agglomeration is an ultra-fast coagulation/agglomeration process. In this section, a numerical analysis of acoustic agglomeration in an inhomogeneous velocity field is carried out by the CFD-sectional algorithm and the numerical simulation is compared with the experimental results reported by Yan et al. [52] regarding acoustic agglomeration in a standing wave field.

5.2.1. Acoustic kernels

The acoustic treatment in a standing-wave agglomerator can achieve higher particle removal efficiency than a travelling field under the same power consumption. As shown in Fig. 7, the acoustic velocity of the air at position *x* and time *t* of a plane standing wave field by the superposition of an incident wave and reflected wave can be described as

$$u_g(x,t) = U_{g0}\sin(kx)\sin(2\pi f t) \tag{25}$$

where, U_{g0} is the acoustic velocity amplitude, k is the wave number and f is the sound frequency.

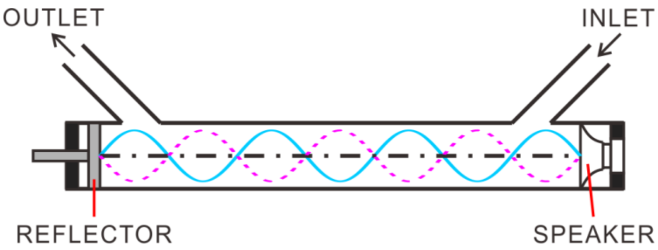

Fig. 7. Illustration of a standing wave field in an acoustic agglomerator.

A variety of mechanisms have been proposed for the interaction between the sound field and suspended particles in aerosols and two primary mechanisms are generally accepted, which are the so-called orthokinetic and hydrodynamic interactions [17]. The acoustic kernels for two particles of diameter d_1 and d_2 which undergo orthorkinetic and hydrodynamic interactions in a standing wave field can be calculated by

$$\beta_s^{OI}(d_1, d_2, x) = 1/2\,(d_1 + d_2)^2 U_{g0}\eta_{12}|\sin(kx)| \tag{26a}$$

$$\beta_s^{HI}(d_1, d_2, x) = \frac{\sqrt{3}\rho_g U_{g0}^2 \sin^2(kx)}{144\pi\mu}\frac{d_1^2 d_2^2}{d_1+d_2} \tag{26b}$$

where, ρ_g is the air density, μ the dynamic viscosity of the air, and η_{12} is the entrainment factor associated with the sound frequency and sound intensity, which are given in Shang et al. [17]. It can be seen that the acoustic kernels in a standing wave field are varied along the propagation direction and accordingly the acoustic agglomeration becomes nonhomogeneous in space. Additionally, the acoustic kernels for orthokinetic and hydrodynamic mechanism are of the order of 10^{-4} cm^3/s or higher, which are much larger than the Brownian kernel (10^{-9} – 10^{-8} cm^3/s). Therefore, the Brownian kernel is negligible in acoustic agglomeration and only the acoustic kernel – the additive combination of Eq. (26a) for orthokinetic interaction and Eq. (26b) for hydrodynamic interaction is considered in the present study. In the present study, the particles are relatively large (0.1 – 10 μm) compared to the mean free path (0.066 μm) of air molecules, and thus, the Cunningham slip correction has insignificant impact on the acoustic kernels and can be neglected. When particles are even smaller to be comparable with the mean free path of air molecules, the slip correction must be taken into account [*].

5.2.2. Governing equations, meshing scheme and numerical settings

In acoustic agglomeration, due to the periodic acoustic wave, both the flow characteristics (transport velocity) and aerosol properties (PSD and concentration) fluctuate periodically with time around their time-average values. Thus, the physical variables in the governing equations consist of two components: the time-averaged value and the fluctuation induced by the acoustic wave within each period of acoustic cycle. Thus, to fully resolve the flow characteristics and aerosol properties over an acoustic period, the flow field induced by the acoustic wave has to be solved within each period of acoustic cycle. However, under such situation, the computation will be too expensive to afford for the current computer capacity when we consider the large number of PDEs, time steps and meshes. Plus, the sampling time of typical aerosol measurement instruments is in the order of tens of seconds, which results in that the fluctuations of the particle size distribution within one acoustic period will be filtered out in measurements. Thus, even if we obtained the flow field and particle size distribution which are time-resolved within one acoustic period, the numerical predictions cannot be validated by the experimental measurements. Therefore, in the present study, we overlook the fluctuations of flow velocity within one acoustic period and solve the time-averaged flow equations without the flow field induced by the acoustic wave. Similarly, the time-averaged population balance equation is solved without considering the fluctuations of PSD within one acoustic period. Similar to the Reynolds averaging in turbulent flows, we only average the periodic fluctuations of physical variables over one acoustic period and the time-dependence due to the operating conditions, such as the inflow, the sound frequency or SPL etc., can be resolved. Since the nonlinear high-order acoustic effects will be significant only for ultrasound frequencies at tens of kilo Hertz [*], we can neglect the high-order term resulting from the averaging process for this case study (1.8 kHz for the sound frequency) without introducing significant errors. As such, the time-averaged governing equations for the flow velocity and population balances share the same form as the expression in Eq. (5), as demonstrated in the Supplemental Material. Hence the developed CFD-sectional solver can be used directly except that the initial and boundary conditions should be set for the time-averaged flow and particle size distribution. In Yan et al. [*], the operating conditions such as the inflow, sound frequency, SPL and PSD etc. at the inlet do not vary with time and thus the agglomeration process after averaging over one acoustic cycle can be regarded as steady state.

In the typical case of Yan et al. [52], the acoustic agglomerator is a duct of 0.04 m width and 0.04 m height. The distance between the inlet and sampling point is equal to 5 wavelengths (0.944 m) and the residence time is 2.5 s. The dimensions of the computation domain for the numerical simulation are identical to those of the agglomerator in the experiments. To test the mesh independence, we study three levels of mesh resolution based on the same meshing scheme as illustrated in Fig. 8: coarse (16 length × 16 width × 180 height), standard (32 length × 32 width × 360 height), and fine (48 length × 48 width × 540 height). Meshes near the walls are elaborately refined to capture the sharp gradients. The aerosol is re-dispersed coal ash with the diameter of the particles between 0.023 μm and 9.314 μm. The sound frequency of the standing wave field is 1.8 kHz and the sound pressure level is 150 dB at every half wavelength from the acoustic source. The operation pressure and temperature are 1 atm and 293 K, respectively. The simulation was performed in parallel on a workstation equipped with 8 CPUs (Intel i7) and the tolerance is 1e-6 for all variables.

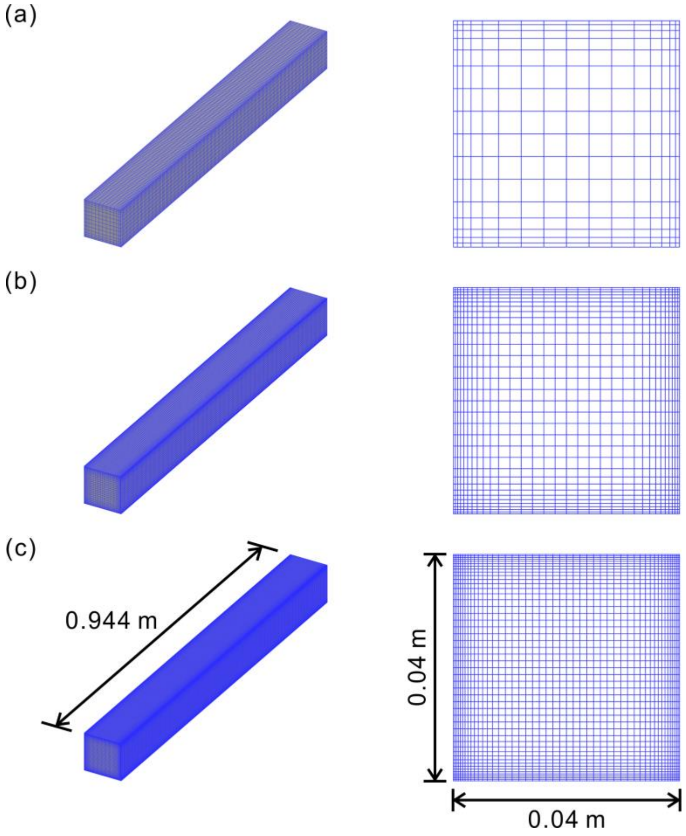

Fig. 8. Illustration of the computation domain and meshing scheme in the mesh independence tests (not to scale). (a) coarse (16 width × 16 depth × 180 length); (b) standard (32 width × 32 depth × 360 length); (c) fine (48 width × 48 depth × 540 length).

Initially, no particles exist inside the acoustic agglomerator. The air velocity at the inlet is calculated from the agglomerator length and residence time of particles. The particle size distribution at the inlet is the same as the initial measurement of Yan et al. [52]. At the outlet, the flow is assumed to be fully developed and all other scalar variables (Q_s) are set as the zero Gradient (Neumann) boundary condition. The air on the walls is non-slip and impenetrable. The particle concentration is set as zero on the walls (Dirichlet boundary condition), which implies that the surface is a perfect sink for deposition, without resuspension or reentrainment of particles. The particle concentration is set as zero on the walls (Dirichlet boundary condition), which implies that the surface is a perfect sink for deposition, without resuspension or reentrainment of particles.

5.2.3. PSD, number concentration and agglomeration efficiency

The average particle size distribution at the outlet of the acoustic chamber is demonstrated in Fig. 9 for the numerical simulations with the coarse (circle), standard (square) and fine (star) meshes in comparison to the experimental measurement (plus). The numerical simulation was conducted under the same initial distribution (diamond) as in the experiments. It can be seen that the simulation results with three levels of meshing resolution reveal a similar trend that the number concentration of the particles in submicron range decreases strikingly, indicating the occurrence of the particle agglomeration. However, there is a noteworthy deviation between the prediction with coarse meshes and the simulation results with the standard or fine meshes. A subtle difference is detected from the standard to fine meshes, confirming that the solution with the standard resolution can be considered "mesh independent". Even though the accuracy is slightly improved for the fine meshes, the computation time is increased dramatically from 2,471 seconds for standard meshes to 19,278 seconds for fine meshes. Therefore, the simulation with standard meshes provides a good trade-off between the accuracy and computational cost, and is used in the following study.

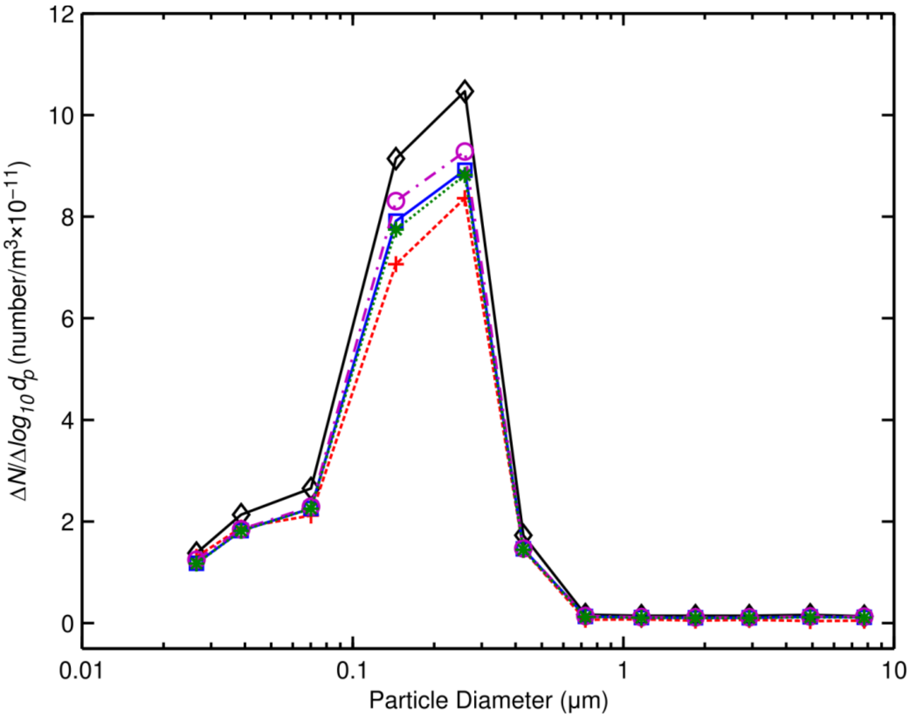

Fig. 9. Simulation results compared with experimental measurements (plus) of the particle size distribution in the acoustic agglomeration for coarse (circle), standard (square) and fine (star) meshes. The initial distribution (diamond) of the aerosol at the chamber inlet is also included.

In Fig. 9, the particle size distribution predicted by the standard or fine meshes shows a satisfactory agreement with the experimental data except that a relatively large deviation is observed for the range from 0.1 to 0.4 μm. In fact, the accuracy of the present CFD-sectional method is also associated with the number of discretization sections for the population balance modeling. As shown in Fig. 9, the particle size distribution in the range of 0.1 – 0.4 μm is varied rapidly with a much steeper slope than that out of this size range. Thus, to ensure the same level of accuracy, the particle size in this range should be discretized with more refined sectioning space, i.e., a larger number of sections are required. However, restricted by the measurement data in experiments [52], we cannot divide the particle size in this range into very fine sections in the simulation. Therefore, the discrepancy between the numerical and experimental results in the range of 0.1 – 0.4 μm is greater than that out of this size range. The deviation in this range is expected to be smaller than what it is currently when finer sectioning spaces are adopted for the population balance modeling. In addition, the air-particle and particle-particle mechanisms for acoustic agglomeration have not been well understood, which also limits the predictive accuracy of the current acoustic kernels in covering a wide range of experimental conditions [*]. Some experimental factors such as the losses of particles in sampling hoses of the measuring devices cannot be incorporated in the simulation, which may be another source of the deviation.

The total number concentration of the particles and the flow velocity are presented in Fig. 10 for the contours along and across the flow direction. It can be seen from Figs. 10a and 10c that the number concentration drops down evidently along the flow direction as the small particles collide and form into agglomerates with the progress of acoustic agglomeration. In the cross section of the duct the number concentration is distributed non-uniformly – equal to its minimum at the wall and to maximum at the core region, and the contours of the number concentration are similar to the velocity field in Figs. 10b and 10d. But the contours are not completely in accordance with each other: From the wall to the core region, the number concentration of the particles undergoes a much steeper increase than the flow velocity.

Although the acoustic kernel is dependent on the propagation distance only, the inhomogeneous velocity and boundary deposition will result in the non-uniformity of the particle distribution across the flow direction. Hence, the complex distribution of the particles is determined by not a single factor, but the combined effects of the velocity field (convection term), wall deposition (boundary condition) and acoustic agglomeration (source term).

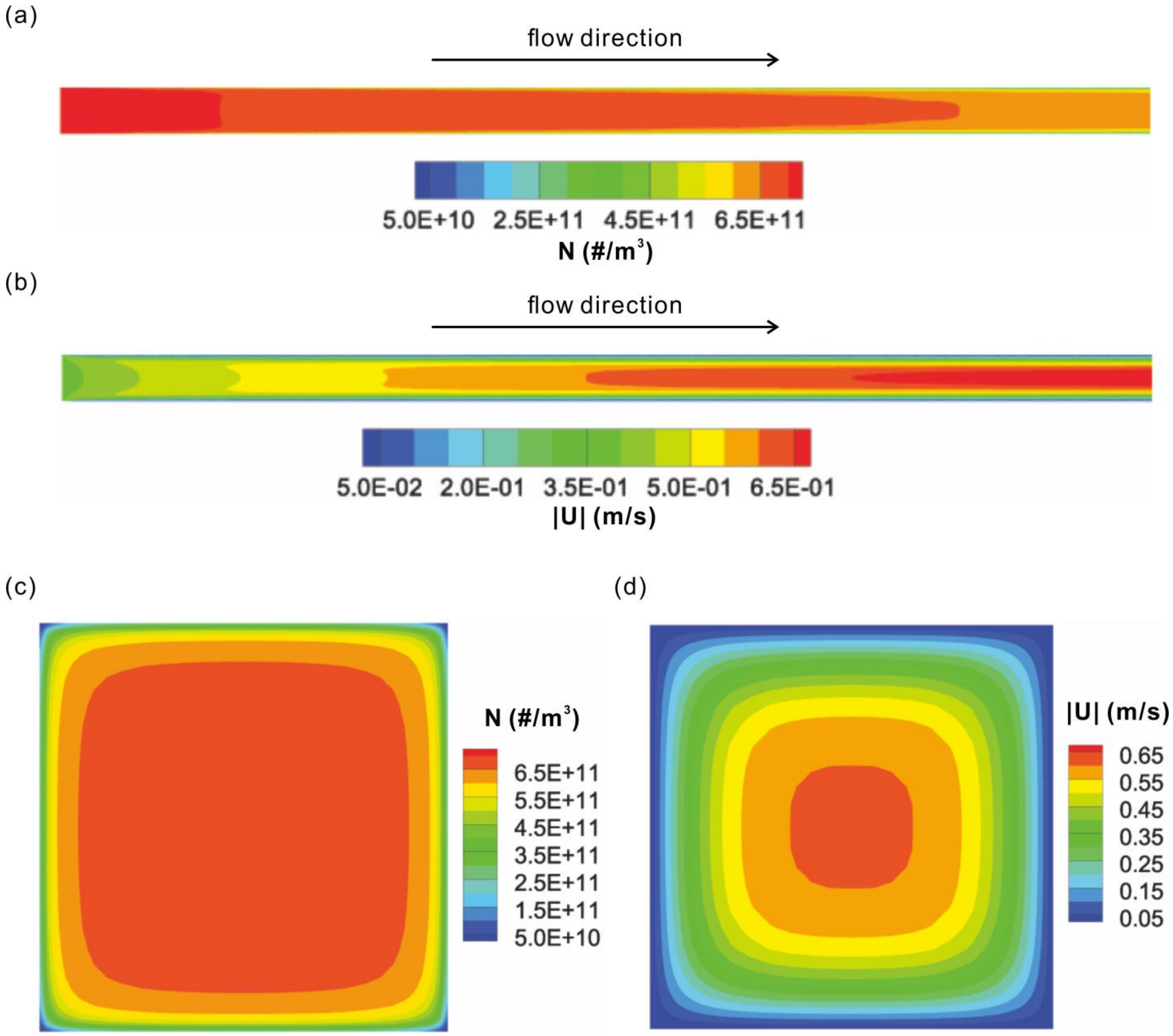

Fig. 10. (a) Spatial distribution of the total number concentration of the particles along the flow direction. (b) Spatial distribution of the velocity field along the flow direction. (c) Spatial distribution of the total number concentration of the particles across the flow direction. (d) Spatial distribution of the velocity field across the flow direction.

For quantitative analysis, the efficiency for acoustic agglomeration can be defined by

$$\eta = (1 - N/N_0) \times 100\% \tag{27}$$

where N and N_0 are the total number concentration of the particles at some position and at the inlet, respectively. The average agglomeration efficiency in the cross section is 18.2%, which is agreeable with the one-dimensional simplified model [17]. To demonstrate its cross-sectional distribution at different positions, *t*he agglomeration efficiency is plotted along two straight lines in the flow direction as shown in Fig. 11a: the center line, L1 (solid), with y=0.02m and z=0.02m and a representative line near the wall, L2 (dashed), with y=0.002m and z=0.002m. As observed in Fig. 11b, the agglomeration efficiency of the particles increases from 0 at the inlet to 27.4 % for L1 and to 10.7% for L2 at the outlet. In closer proximity to the wall, the flow velocity is slower and then the particles experience a longer time of acoustic agglomeration. Thus, the acoustic agglomeration efficiency along L1 is larger than that along L2. It is also worth noting that the agglomeration efficiency is not increased linearly but displays node-antinode alternations in an intermittent way, which is ascribed to the spatial alternation of the acoustic kernel from the velocity node to antinode.

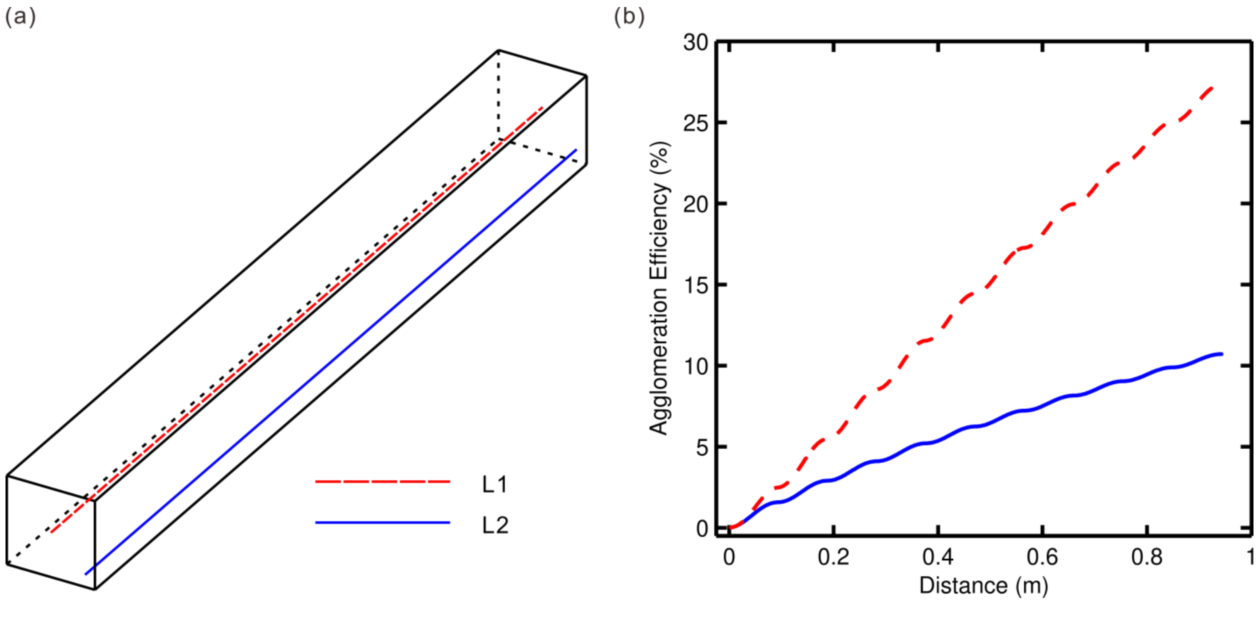

Fig. 11. (a) Demonstration of the positions of the two straight lines along the flow direction: L1 (center line) for the dashed line and L2 (near wall) for the solid line. (b) The predicted efficiency of acoustic agglomeration along the flow direction for L1 (dashed) and L2 (solid).

A further investigation was conducted by varying the SPL from 120 dB to 152 dB while keeping the frequency fixed at 1.8 kHz. The numerical results and the experimental data were presented in Fig. 12a. It is observed that the increase of the sound pressure level can effectively enhance the agglomeration efficiency for both numerical simulation and experiments: The measured agglomeration efficiency in experiments increases from 6.2% at 120 dB to 21.5% at 152 dB while the predicted value increases from 5.8% at 120 dB to 20.6% at 152 dB. The predicted agglomeration efficiency is found to be in good agreement with the experimental data, which confirms the predictive capability of the present CFD-sectional model for the spatially inhomogeneous coagulation/agglomeration process coupled with a fluid flow. Besides, the predicted particle size distribution at 131 dB and 152 dB are also presented in Fig. 12b. The profiles of the particle size distribution for two cases are similar while the decreased area under the PSD curve with increasing SPL indicates the reduction of the number concentration of the particles, which is in accordance with the increasing agglomeration efficiency in Fig. 12a.

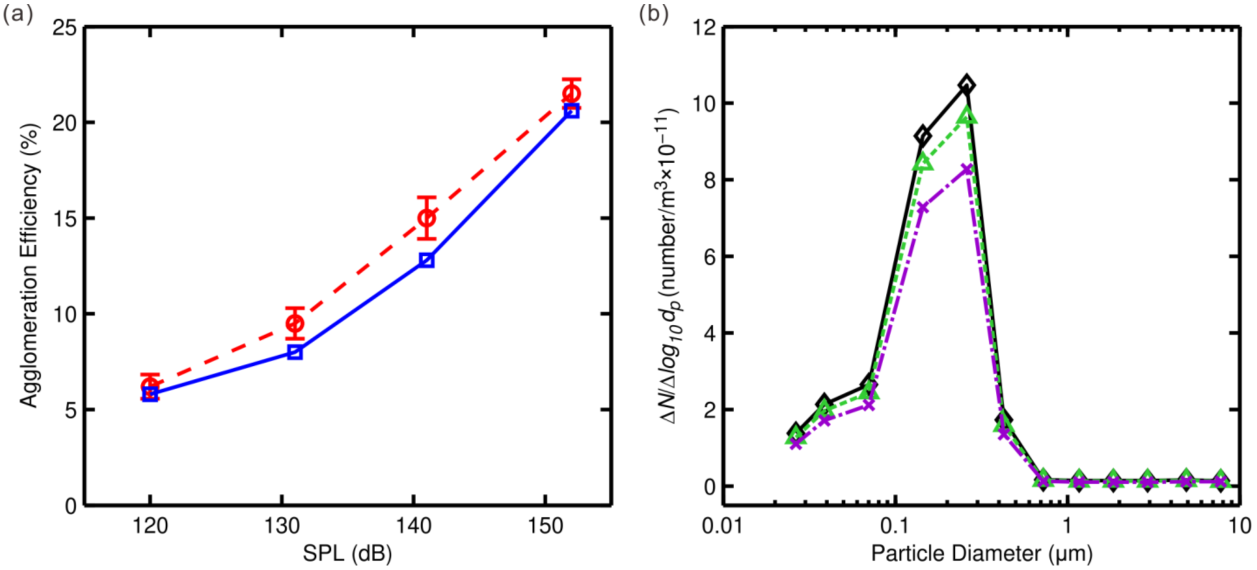

Fig. 12. (a) Numerical results (square) and experimental data (circle) of the agglomeration efficiency at varied SPL. (b) Comparison of the predicted particle size distribution at 131 dB (triangle) and 152 dB (cross). The acoustic frequency is fixed at 1.8 kHz for all cases.

The particle distribution and acoustic agglomeration process shown in Figs. 9-12 demonstrates that the present CFD-sectional model is capable to predict more details of the standingconditioned acoustic agglomeration than the conventional temporal model and the spatial inhomogeneity further confirms the rationality of multi-dimensional population balance modeling in acoustic agglomeration.

5.2.4 Wall deposition

According to the Fick's law, the flux of particle deposition caused by the Brownian and turbulent diffusion is calculated by $\vec{J} = -[(D_B + D_T)\nabla N]_{wall}$, where D_B and D_T are the Brownian and turbulent diffusivity, respectively.

To quantify the effect of wall deposition, we define a coefficient of deposition loss as,

$$DL = \dot{N}_{dep}/\dot{N}_{inlet} \times 100\% \qquad (*)$$

where, $\dot{N}_{dep}$ is the deposition rate of particles in total and $\dot{N}_{inlet}$ is the inflow rate of particles entering the chamber and they are calculated by

$$\dot{N}_{dep} = \iint_{wall} \vec{J} \cdot d\vec{S}$$

$$\dot{N}_{inlet} = \iint_{inlet} \vec{J} \cdot d\vec{S}$$

The coefficient of the deposition loss of particles is presented in Fig. 13 as a function of the particle diameter. It can be seen that the maximum deposition loss occurs at the smallest particles, only accounting for 0.11% of the inflow particles. The deposition loss caused by the Brownian and turbulent diffusion is reduced with the increasing particle size and becomes negligible for particles larger than 0.2 μm in diameter. Thus, the loss of particles due to the wall deposition is very small, and has an insignificant impact on the acoustic agglomeration in the present study.

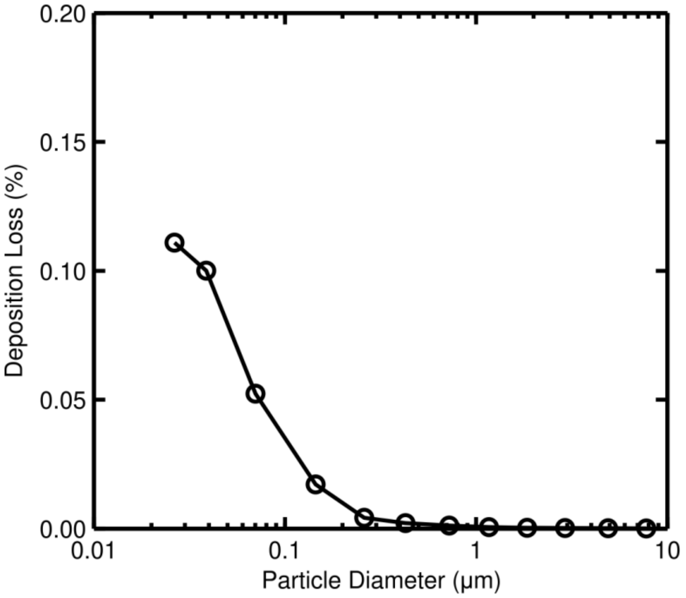

Fig. 13. The dependence of the deposition loss on the particle size at 1.8 kHz and 150 dB.

6. Conclusions

In summary, a CFD-sectional algorithm that solves the spatially inhomogeneous population balance equation coupled with multi-dimensional flow dynamics is presented. The population balance modeling which includes convective and diffusive transport of aerosols is based on the sectional method of Gelbard and Seinfeld [15]. The solution of the section PBE is incorporated into a standard CFD framework for a laminar or turbulent flow. The following findings can be summarized from the present study:

1) An adaptive numerical quadrature is proposed to specify the sectional coefficients. By adaptively reducing the integration domain, the numerical quadrature achieves high computation accuracy in a convenient and economic way. The inter-equation coupling associated with the sectional PBEs is treated by the hybrid-segregated procedure to avoid the lagging effect. The source term is linearized by the operator splitting method into an explicit and an implicit part, which combines the merits of computational economy of explicit schemes and stability of implicit schemes. The solution of the sectional population balance equation is incorporated into the standard CFD simulation of incompressible flows such as the SIMPLE algorithm or PISO algorithm. Turbulence simulation can also be included to study the coagulation or diffusion in a turbulent flow.

2) The computation accuracy of the modified numerical quadrature with adaptive limits is shown to be greatly improved for the same number of integration nodes. The present CFD-sectional algorithm is benchmarked by an analytical solution of Brownian coagulation/agglomeration of particles in the continuum regime. The prediction of the CFD-sectional modeling is in good agreement with the self-preserving distribution. Satisfactory results are obtained concerning the prediction of the geometric mean diameter and geometric standard deviation of the particle size distribution.

3) The acoustic agglomeration in a standing wave field is simulated as a case study. The predicted particle size distribution agrees well with the experimental data, which demonstrates the capability of the CFD-sectional algorithm in simulating ultra-fast coagulation/agglomeration processes. On this basis, the particles are found to be distributed non-uniformly in the duct due to the combined effects of the inhomogeneous velocity field, wall deposition and acoustic agglomeration. Besides, the agglomeration efficiency is found to increase in an intermittent way along the flow direction and differ with the varied position in the cross section of the duct.

Although the developed CFD-sectional algorithm is limited to the phenomena of aerosol coagulation, convection, diffusion and deposition, its extension to the nucleation and condensation is conceptually straightforward. However, the present algorithm overlooks the impact of the aerosol dynamics on the mass and momentum transfer of the carrier fluids, which makes it suitable for the dilute particle-laden flows. The two-way coupling between the population balance equation and the fluid dynamics will be our goal in future.

Acknowledgements

This study is supported by the Republic of Singapore's Ministry of Education MOE2016-T2-1-063.

References

[1] R.I. Jeldres, P.D. Fawell, B.J. Florio, Population balance modelling to describe the particle aggregation process: A review, Powder Technol. 326 (2018) 190-207.

[2] C. Shu, A. Chatterjee, W. Hu, D. Ramkrishna, Modeling of gene regulatory processes by population-mediated signaling: New applications of population balances, Chem. Eng. Sci. 70 (2012) 188-199.

[3] M. Yu, J. Lin, T.L. Chan, Numerical simulation of nanoparticle synthesis in diffusion flame reactor, Powder Technol. 181 (2008) 9-20.

[4] T.L. Chan, S. Liu, Y. Yue, Nanoparticle formation and growth in turbulent flows using the bimodal TEMOM, Powder Technol. 323 (2018) 507-517.

[5] R.I. Jeldres, F. Concha, P.G. Toledo, Population balance modelling of particle flocculation with attention to aggregate restructuring and permeability, Adv. Colloid Interface Sci. 224 (2015) 62-71.

[6] M. Hussain, J. Kumar, E. Tsotsas, Modeling aggregation kinetics of fluidized bed spray agglomeration for porous particles, Powder Technol. 270 (2015) 584-591.

[7] D. Barrasso, A.E. Hagrasy, J.D. Litster, R. Ramachandran, Multi-dimensional population balance model development and validation for a twin screw granulation process, Powder Technol. 270 (2015) 612-621.

[8] D. Mitrakos, E. Hinis, C. Housiadas, Sectional modeling of aerosol dynamics in multi-dimensional flows, Aerosol Sci. Technol. 41 (2007) 1076-1088.

[9] R. McGraw, Description of aerosol dynamics by the quadrature method of moments, Aerosol Sci. Technol. 27 (1997) 255-265.

[10] M. Yu, J. Lin, T.L. Chan, A new moment method for solving the coagulation equation for particles in Brownian motion, Aerosol Sci. Technol. 42 (2008) 705-713.

[11] M. Yu, J. Lin, M. Seipenbusch, J. Cao, Verification of size-resolved population balance modeling for engineered nanoparticles under high concentration, Chem. Eng. J. 323 (2017) 592-604.

[12] H. Zhao, F.E. Kruis, C. Zheng, A differentially weighted Monte Carlo method for two-component coagulation, J. Comput. Phys. 229 (2010) 6931-6945.

[13] S. Liu, T.L. Chan, A coupled CFD-Monte Carlo method for simulating complex aerosol dynamics in turbulent flows, Aerosol Sci. Technol. 51 (2017) 269-281.

[14] H.M. Liu, T.L. Chan, Two-component aerosol dynamic simulation using differentially weighted operator splitting Monte Carlo method, Appl. Math. Model. 62 (2018) 237-253.

[15] F. Gelbard, J.H. Seinfeld, The general dynamic equation for aerosols. Theory and application to aerosol formation and growth, J. Colloid Interface Sci. 68 (1979) 363-382.

[16] D. Katoshevski, J.H. Seinfeld, Analytical-numerical solution of the multicomponent aerosol general dynamic equation – with coagulation, Aerosol Sci. Technol. 27 (1997) 550-556.

[17] X. Shang, B.F. Ng, M.P. Wan, J. Xiong, S. Arikrishnan, Numerical investigation of spatially nonhomogeneous acoustic agglomeration using sectional algorithm, Aerosol Sci. Technol. 52 (2018) 872-885.

[18] S. Kumar, D. Ramkrishna, On the solution of population balance equations by discretization-I. A fixed pivot technique, Chem. Eng. Sci. 51 (1996) 1311-1332.

[19] J. Kumar, G. Warnecke, M. Peglow, S. Heinrich, Comparison of numerical methods for solving population balance equations incorporating aggregation and breakage, Powder Technol. 189 (2009) 218-229.

[20] J. Kumar, M. Peglow, G. Warnecke, S. Heinrich, An efficient numerical technique for solving population balance equation involving aggregation, breakage, growth and nucleation, Powder Technol. 182 (2008) 81-104.

[21] F. Stratmann, E.R. Whitby, Numerical solution of aerosol dynamics for simultaneous convection, diffusion and external forces, J. Aerosol Sci. 20 (1989) 437-440.

[22] F.E. Kruis, K.A. Kusters, S.E. Pratsinis, B. Scarlett, A simple model for the characteristics of aggregate particles undergoing coagulation and sintering, Aerosol Sci. Technol. 19 (1993) 514-526.

[23] V.S. Buddhiraju, V. Runkana, Simulation of nanoparticle synthesis in an aerosol flame reactor using a coupled flame dynamics-monodisperse population balance model, J. Aerosol Sci. 43 (2012) 1-13.

[24] H. Muhlenweg, A. Gutsch, A. Schild, S.E. Pratsinis, Process simulation of gas-to-particle-synthesis via population balances: Investigation of three models, Chem. Eng. Sci. 57 (2002) 2305-2322.

[25] B. Schwade, P. Roth, Simulation of nano-particle formation in a wall-heated aerosol reactor including coalescence, J. Aerosol Sci. 34 (2003) 339-357.

[26] A. Passalacqua, F. Laurent, E. Madadi-Kandjani, J.C. Heylmun, R.O. Fox, An open-source quadrature-based population balance solver for OpenFOAM, Chem. Eng. Sci. 176 (2018) 306-318.

[27] T.T. Nguyen, F. Laurent, R.O. Fox, M. Massot, Realizable second-order finite-volume schemes for the advection of moment sets of the particle size distribution, J. Comput. Phys. 325 (2016) 129-156.

[28] F. Fan, M. Zhang, Z. Peng, J. Chen, M. Su, B. Moghtaderi, E. Doroodchi, Direct simulation Monte Carlo method for acoustic agglomeration under standing wave condition, Aerosol Air Qual. Res. 17 (2017) 1073-1083.

[29] J. Pyykonene, J. Jokineimi, Computational fluid dynamics based sectional aerosol modelling schemes, J. Aerosol Sci. 31 (2000) 531-550.

[30] J.I. Jeong, M. Choi, A sectional method for the analysis of growth of polydisperse non-spherical particles undergoing coagulation and coalescence, J. Aerosol Sci. 32 (2001) 565-582.

[31] J.I. Jeong, M. Choi, Analysis of non-spherical polydisperse particle growth in a two-dimensional tubular reactor, J. Aerosol Sci. 34 (2003) 713-732.

[32] E.M.A. Frederix, A.K. Kuczaj, M. Nordlund, A.E.P. Veldman, B.J. Geurts, Application of the characteristics-based sectional method to spatially varying aerosol formation and transport, J. Aerosol Sci. 104 (2017) 123-140.

[33] S. Kommu, B. Khomami, P. Biswas, Simulation of aerosol dynamics and transport in chemically reacting particulate matter laden flows. Part I: Algorithm development and validation, Chem. Eng. Sci. 59 (2004) 345-358.

[34] S. Kommu, B. Khomami, P. Biswas, Simulation of aerosol dynamics and transport in chemically reacting particulate matter laden flows. Part II: Application to CVD reactors, Chem. Eng. Sci. 59 (2004) 359-371.

[35] S.K. Friedlander, Smoke, Dust, and Haze: Fundamentals of Aerosol Dynamics, second ed., Oxford University Press, New York, 2000.

[36] P.J. Adams, J.H. Seinfeld, Predicting global aerosol size distributions in general circulation models, J. Geophys. Res. 107 (2002) AAC 4-1.

[37] M. Kajino, R.C. Easter, S.J. Ghan, Modal Bin Hybrid Model: A surface area consistent, triple-moment sectional method for use in process-oriented modeling of atmospheric aerosols, J. Geophys. Res. Atmos. 118 (2013) 10011–10040.

[38] J.D. Landgrebe, S.E. Pratsinis, A discrete-sectional model for particulate production by gas-phase chemical reaction and aerosol coagulation in the free-molecular regime, J. Colloid Interface Sci. 139 (1990) 63-86.

[39] C. Wu, P. Biswas, Study of numerical diffusion in a discrete-sectional model and its application to aerosol dynamics simulation, Aerosol Sci. Technol. 29 (1998) 359-378.

[40] M. Vanni, Approximate population balance equations for aggregation-breakage processes, J. Colloid Interface Sci. 221 (2000) 143–160.

[41] S.V. Patankar, Numerical Heat Transfer and Fluid Flow, first ed., Hemisphere Publishing Corporation, New York, 1980.

[42] R.I. Issa, Solution of the implicitly discretized fluid flow equations by operator-splitting, J. Comput. Phys. 62 (1986) 40-65.

[43] A.C.K. Lai, W.W. Nazaroff, Modeling indoor particle deposition from turbulent flow onto smooth surfaces, J. Aerosol Sci. 31 (2000) 463-476.

[44] W.M. Deen, Analysis of Transport Phenomena, first ed., Oxford University Press, New York, 1998.

[45] S.A. Orzag, M. Israeli, Numerical simulation of viscous incompressible flows, Annu. Rev. Fluid Mech. 5 (1974) 281-318.

[46] H. Jasak, Error analysis and estimation for the finite volume method with applications to fluid flows, (Ph.D. Dissertation) London, UK: Imperial College London, 1996.

[47] H.A. van der Vorst, Bi-CGSTAB: A fast and smoothly converging variant of Bi-CG for the solution of nonsymmetric linear systems, SIAM J. Sci. Comput. 13 (1992) 631-644.

[48] OpenFOAM Foundation, OpenFOAM User Guide. https://openfoam.org/, 2017.

[49] K.W. Lee, Y.J. Lee, D.S. Han, The log-normal size distribution theory for Brownian coagulation in the low Knudsen number regime, J. Colloid Interface Sci. 188 (1997) 486-492.

[50] W.T. Yuen, S.C. Fu, J.K.C. Kwan, C.Y.H. Chao, The use of nonlinear acoustics as an energy-efficient technique for aerosol removal, Aerosol Sci. Technol. 48 (2014) 907-915.

[51] B.F. Ng, J.W. Xiong, M.P. Wan, Application of acoustic agglomeration to enhance air filtration efficiency in air-conditioning and mechanical ventilation (ACMV) systems, PLOS ONE 12 (2017) e0178851.

[52] J. Yan, L. Chen, L. Yang, Combined effect of acoustic agglomeration and vapor condensation on fine particles removal, Chem. Eng. J. 290 (2016) 319-327.

[53] B. Zhao, M. Li, L.Y. Wang, D. Katoshevski, T.S. Chung, Particle grouping and agglomeration assisted by damper oscillation systems, Sep. Purif. Technol. 207 (2018) 12-19.

Figure Captions

Fig. 1. Illustration of the integration limits of ${}^{1}\beta_{i,j,l}$ for the case of: (a) $i = l - 1, j < l - 1$ and (b) $i < l - 1, j = l - 1$. The black shaded area shows the "goal" region and v_{l-1} and v_l represent the lower and upper boundaries of the agglomerating section.

Fig. 2. Illustration of the integration limits of ${}^{2}\beta_{i,l}$ for the case of: (a) $\theta(u + v > v_l)$ and (b) $\theta(v_{l-1} < u + v < v_l)$. The black shaded area shows the "goal" region and v_{l-1} and v_l represent the lower and upper boundaries of the agglomerating section.

Fig. 3. Illustration of the integration limits of ${}^{3}\beta_{l,l}$. The black shaded area shows the “goal” region and v_{l-1} and v_l represent the lower and upper boundaries of the agglomerating section.

Fig. 4. Schematic representation of the CFD-sectional algorithm.

Fig. 5. Comparison between the self-preserving particle distribution (dashed line) and the prediction of CFD-sectional algorithm (stairs) for an aerosol of particles undergoing Brownian coagulation/agglomeration in the continuum regime at 24 hours. The initial distribution is denoted by the solid line.

Fig. 6. Illustration of the computation domain and meshing scheme in the simulation (not to scale). (a) Global meshing (b) Near-wall Refinement.

Fig. 7. Simulation results (square) compared with experimental measurements (plus) of the particle size distribution in a standing wave field. The initial distribution (diamond) of the aerosol at the chamber inlet is also included.

Fig. 8. (a) Spatial distribution of the total number concentration of the particles along the flow direction. (b) Spatial distribution of the total number concentration of the particles across the flow direction. (c) Spatial distribution of the velocity field across the flow direction.

Fig. 9. (a) Demonstration of the positions of the two straight lines along the flow direction: L1 (center line) for the dashed line and L2 (near wall) for the solid line. (b) The predicted efficiency of acoustic agglomeration along the flow direction for L1 (dashed) and L2 (solid).